

Orbital- and Millennial-Scale Variability in Northwest African Dust Emissions Over the Past 67,000 years

Christopher W. Kinsley¹, Louisa Irene Bradtmiller², David McGee³, Michael Galgay², Jan-Berend Willem Stuut⁴, Rik Tjallingii⁵, Gisela Winckler⁶, and Peter B. deMenocal⁷

¹Massachusetts Institute of Technology

²Macalester College

³MIT

⁴NIOZ - Royal Netherlands Institute for Sea Research, and Utrecht University

⁵GFZ German Research Centre for Geosciences

⁶Columbia University

⁷Lamont-Doherty Earth Observatory

November 22, 2022

Abstract

Reconstructions of aeolian dust flux to West African margin sediments can be used to explore changing atmospheric circulation and hydroclimate over North Africa on millennial to orbital timescales. Here, we extend West African margin dust flux records back to 35 ka in a transect of core sites from 19°N to 27°N, and back to 67 ka at Ocean Drilling Program (ODP) Hole 658C, in order to explore the interplay of orbital and high-latitude forcings on North African climate and make quantitative estimates of dust flux during the core of the Last Glacial Maximum (LGM). The ODP 658C record shows a “Green Sahara” interval from 60 to 50 ka during a time of high Northern Hemisphere summer insolation, with dust fluxes similar to levels during the early Holocene African Humid Period, and an abrupt peak in flux during Heinrich event 5a (H5a). Dust fluxes increase from 60 to 35 ka while the high-latitude Northern Hemisphere cools, with peaks in dust flux associated with North Atlantic cool events. From 35 ka through the LGM dust deposition decreases in all cores, and little response is observed to low-latitude insolation changes. Dust fluxes at sites north of 20°N were near late Holocene levels during the LGM time slice, suggesting a more muted LGM response than observed in mid-latitude dust sources. Records along the northwest African margin suggest important differences in wind responses during different stadials, with maximum dust flux anomalies centered south of 20°N during H1 and north of 20°N during the Younger Dryas.

1 **Orbital- and Millennial-Scale Variability in Northwest African Dust Emissions Over**
2 **the Past 67,000 years**

3
4
5 **Christopher W. Kinsley¹, Louisa I. Bradtmiller², David McGee¹, Michael Galgay², Jan-**
6 **Berend Stuut^{3,4}, Rik Tjallingii⁵, Gisela Winckler⁶, and Peter B. deMenocal⁶**

7
8 ¹Department of Earth, Atmospheric and Planetary Sciences, Massachusetts Institute of
9 Technology, Cambridge, MA, USA, ²Department of Environmental Studies, Macalester College,
10 St. Paul, MN, USA, ³NIOZ Royal Netherlands Institute for Sea Research, Texel, The
11 Netherlands, ⁴Faculty of Science, Department of Earth Sciences, Vrije Universiteit Amsterdam,
12 Amsterdam, The Netherlands, ⁵GFZ German Research Centre for Geosciences, Section 'Climate
13 Dynamics and Landscape Evolution', Potsdam, Germany, ⁶Lamont-Doherty Earth Observatory,
14 Columbia University, Palisades, NY, USA

15 Corresponding author: Christopher W. Kinsley (ckinsley@mit.edu)

16
17 **Key Points:**

- 18 • Coherent dust flux changes along the NW African margin and in the central North
19 Atlantic over the last 67 ka
- 20 • Abrupt dust flux variations on millennial timescales similar to N Atlantic stadials related
21 to high latitude forcing of African climate
- 22 • Green Sahara interval (60-50 ka) recorded by low dust fluxes to ODP 658C showing an
23 orbitally-forced strengthening of monsoon during MIS 3
- 24
25
26
27
28
29
30
31

32 **Abstract**

33 Reconstructions of aeolian dust flux to West African margin sediments can be used to explore
34 changing atmospheric circulation and hydroclimate over North Africa on millennial to orbital
35 timescales. Here, we extend West African margin dust flux records back to 35 ka in a transect of
36 core sites from 19°N to 27°N, and back to 67 ka at Ocean Drilling Program (ODP) Hole 658C, in
37 order to explore the interplay of orbital and high-latitude forcings on North African climate and
38 make quantitative estimates of dust flux during the core of the Last Glacial Maximum (LGM).
39 The ODP 658C record shows a “Green Sahara” interval from 60 to 50 ka during a time of high
40 Northern Hemisphere summer insolation, with dust fluxes similar to levels during the early
41 Holocene African Humid Period, and an abrupt peak in flux during Heinrich event 5a (H5a).
42 Dust fluxes increase from 60 to 35 ka while the high-latitude Northern Hemisphere cools, with
43 peaks in dust flux associated with North Atlantic cool events. From 35 ka through the LGM dust
44 deposition decreases in all cores, and little response is observed to low-latitude insolation
45 changes. Dust fluxes at sites north of 20°N were near late Holocene levels during the LGM time
46 slice, suggesting a more muted LGM response than observed in mid-latitude dust sources.
47 Records along the northwest African margin suggest important differences in wind responses
48 during different stadials, with maximum dust flux anomalies centered south of 20°N during H1
49 and north of 20°N during the Younger Dryas.

50

51 **1 Introduction**

52 Records of mineral dust emissions from the Sahara Desert are essential for understanding
53 past changes in North African climate, and are tightly linked to the strength of the West African
54 monsoon (deMenocal, 1995; deMenocal, et al., 2000; Skonieczny et al., 2019; Wang, et al.,
55 2015). Wind speed and aridity variations are expressed as fluctuations in the amount of dust
56 exported from the North African continent to the Atlantic Ocean, meaning that downcore
57 measurement of dust flux to North Atlantic sediments allows an integrated reconstruction of how
58 winds and aridity respond to climate changes.

59 In the present day, North African dust outbreak events transport dust over the northwest
60 African continental margin and Atlantic Ocean throughout the year. Observational records from
61 marine sediment traps and atmospheric dust samplers suggest that maximum dust deposition
62 along the northwest African margin occurs in winter and spring (Bory & Newton, 2000;

63 Chiapello et al., 1995; Ratmeyer et al., 1999; Skonieczny et al., 2013). Combining air parcel
64 back trajectory modeling with dust provenance (Friese et al., 2017; Skonieczny et al., 2013) and
65 grain size measurements (van der Does et al., 2016) suggests that winter dust is transported in
66 low-level trade winds from relatively proximal locations, including the coastal region of Western
67 Sahara and western Mauritania (see Scheuvens et al., 2013 for a compilation of PSA locations).
68 Interannual peaks in winter dust emissions are attributed to southward movement of the ITCZ
69 and increased surface winds over North African dust source regions, with a minor role of
70 reduced Sahel rainfall (Doherty et al., 2012).

71 During summer, dust is transported from source regions closer to the center of the
72 continent (e.g., Libya) and uplifted at the coast by a cool marine inversion layer and transported
73 by the upper level (~1.5-4.5 km) Saharan Air Layer (Carlson & Prospero, 1972). Satellite
74 observations of atmospheric dust loading and fluxes show peak dust transport across the Atlantic
75 in summer (Ridley et al., 2012; Yu et al., 2015); however, relatively little of this dust appears to
76 be deposited on the northwest African margin (Skonieczny et al., 2013). As a result, our records
77 are likely to be biased toward winter dust emissions from the western Sahara Desert. To address
78 this potential seasonal and spatial bias in our interpretations, in section 4.1 we compare data from
79 our African margin sites with data from a distal core site that represents predominantly summer
80 dust deposition from interior African source regions (Middleton et al., 2018).

81 Paleoclimate proxy records and geochemical tools have been used to extend the record of
82 variability of dust transport to the margin beyond the observational record, which exists only
83 from the mid-1960s (Prospero & Lamb, 2003). Records of the last 20 ka (ka: thousand years
84 before present) were developed using sediments from Ocean Drilling Program (ODP) Hole 658C
85 by deMenocal et al. (2000) and Adkins et al. (2006). Later work demonstrated that the variations
86 in this core were coherent along the northwest African margin between 19°N and 27°N (McGee
87 et al., 2013) and were observed across the Atlantic Basin in the Bahamas and central Atlantic as
88 well (Williams et al., 2016). These reconstructions show an abrupt transition from a time of high
89 dust accumulation during the deglaciation to a sustained period of low dust accumulation
90 between 12 and 5 ka. This low-dust period is known as the African Humid Period (AHP) and is
91 marked by an abrupt onset and termination, followed by a more gradual increase of dust
92 accumulation toward the present. Comparison of these dust records with other climate proxy
93 records of North African climate shows that the AHP marks a “Green Sahara”, when the Sahara

94 Desert received high rainfall supporting diverse and widespread vegetation, permanent lakes, and
95 human populations (McGee & deMenocal, 2017, and references therein), with accompanying
96 continental runoff (Drake et al., 2010; Skonieczny et al., 2015; Weldeab et al., 2014). The AHP
97 occurred when Northern Hemisphere summer insolation was increased relative to the present due
98 to precessional variation, which has been shown through modeling efforts to increase the extent
99 and intensity of the monsoon system (Battisti et al., 2014; Braconnot et al., 2012; Kutzbach,
100 1981; Tjallingii et al., 2008). There is also evidence that trade wind strength was decreased over
101 the West African margin during the AHP, as evidenced by decreased upwelling-related biogenic
102 fluxes to margin sediments and increased sea surface temperatures (SSTs) along the margin
103 (Adkins et al., 2006; Bradtmiller et al., 2016). These findings over the AHP highlight two of the
104 controls on changes to dust flux from North Africa, aridity and wind strength, and the
105 importance of considering the interplay between the two.

106 These studies also began to elucidate dramatic intervals of rapid and high-amplitude
107 changes to climate and dust transport in this region over far shorter timescales, punctuating the
108 orbitally-forced record at a millennial scale. During abrupt Northern Hemisphere cooling events
109 such as Heinrich event 1 (H1) (~18.0 to 15 ka), and the Younger Dryas (YD) episode (12.8 to
110 11.7 ka; Rasmussen et al., 2006) abrupt increases in dust flux have been recorded at multiple
111 sites over the margin, with fluxes reaching the highest values of their respective records during
112 these events (Adkins et al., 2006; McGee et al., 2013; Mulitza et al., 2008).

113 Multiple studies have linked North Atlantic cooling to increases in northeasterly winds
114 over North Africa (deMenocal et al., 1993; McGee et al., 2018; Meyer et al., 2013; Mulitza et al.,
115 2008; Tjallingii et al., 2008). Cooling of winter SSTs and expansion of sea ice in the North
116 Atlantic shift the Atlantic ITCZ to the south, weakening the monsoon and increasing trade wind
117 strength, leading to an increase of dust export (Liu et al., 2014; Murphy et al., 2014). Consistent
118 with this finding from models, northwest African margin sediments record increases in the
119 accumulation of biogenic opal and organic carbon during these cold events, suggesting increased
120 wind-driven upwelling (Adkins et al., 2006; Bradtmiller et al., 2016; Romero et al., 2008). A
121 weakening of monsoon rainfall during North Atlantic cooling events also shifts the Sahel-Sahara
122 boundary south (Collins et al., 2013), potentially opening up new dust source areas and further
123 contributing to the increase in dust emissions during these events. These high-resolution studies
124 provide evidence for a North Atlantic high-latitude control causing abrupt changes to

125 atmospheric circulation and North African climate on millennial timescales, in addition to the
126 low-latitude orbital regulation of African monsoonal climate.

127 Recent efforts by Skonieczny et al. (2019) have shown a high correlation of Saharan dust
128 flux, calculated using ^{230}Th normalization, with summer insolation over the last 240 ka,
129 confirming low-latitude pacing of northwest African dust fluxes at 18°N spanning at least the
130 last two glacial cycles for sediment core MD03-2705. Low sedimentation rates for core MD03-
131 2705, which is adjacent to ODP Hole 658C, precluded detailed study of potential millennial scale
132 controls on North African climate over this longer time frame. Here we present northwest
133 African margin dust flux records from core sites with higher sedimentation rates ($5\text{-}10\text{ cm kyr}^{-1}$)
134 to explore the combined effects of high-latitude and orbital forcing of African climate extending
135 back to 67 ka. Probing this time period allows us to examine over multiple precessional cycles
136 the impact of high-latitude and summer insolation forcing on dust export, and to provide
137 quantitative estimates of dust flux during the core of the LGM time slice. We also explore how
138 millennial-scale increases in dust emission varied along a north-south transect of cores,
139 providing insight into the spatial distribution of wind and aridity changes during these events.
140 Drawing on the mechanistic links between regional climate and dust export, we aim to deepen
141 understanding of changing climate of the North Africa region over the past 67 ka.

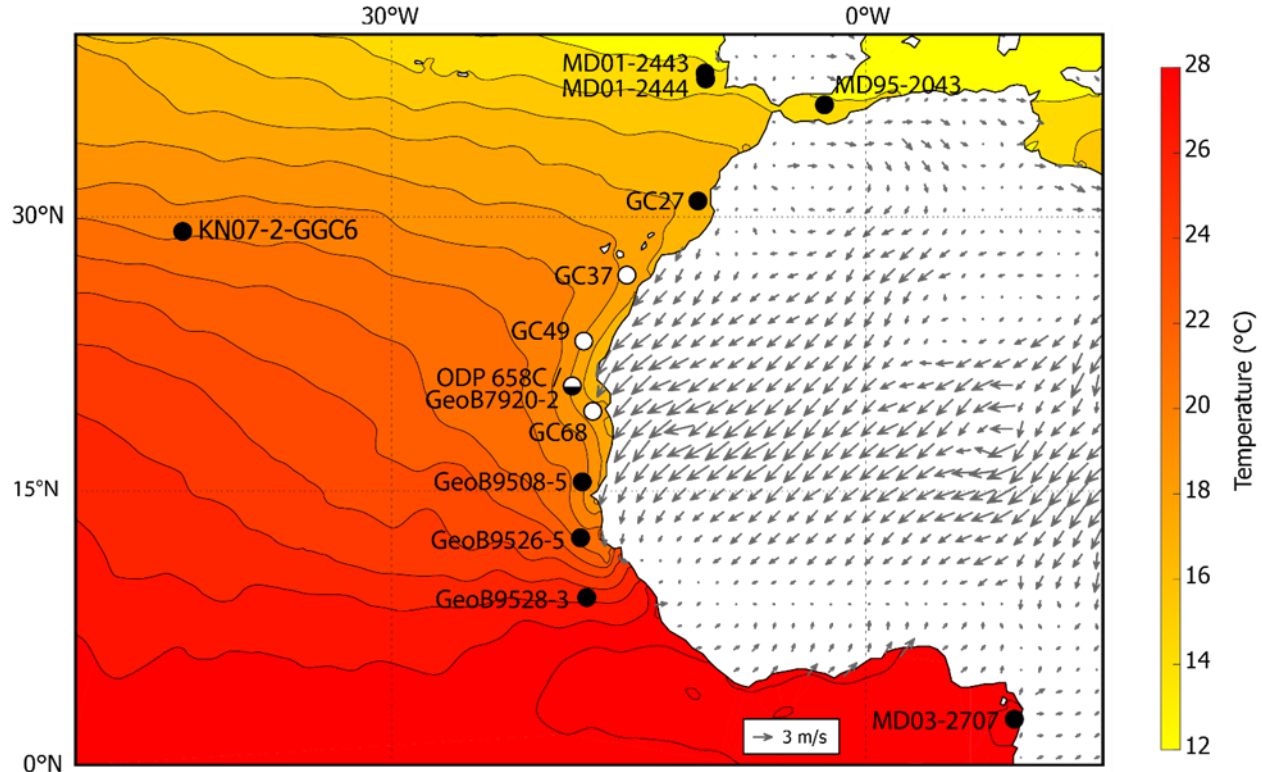
142

143 **2 Methods and Core Sites**

144 2.1 Core Locations

145 A meridional transect of 4 core sites between 27°N and 19°N were used in this study
146 (Figure 1). These sites have been used to monitor past variations in northwest African climate
147 (Bradtmitter et al., 2016; McGee et al., 2013; Williams et al., 2016), as they represent North
148 African dust emissions to the tropical North Atlantic. The southernmost core lies on the northern
149 edge of the modern day winter dust plume (e.g., Mulitza et al., 2008; Skonieczny et al., 2019; Yu
150 et al., 2015) meaning the sites are sensitive to latitudinal variations in dust export. The three
151 gravity cores GC37, GC49, and GC68, were taken by the R/V Oceanus during the 2007
152 Changing Holocene Environments of the Eastern Tropical Atlantic (CHEETA) cruise (OC437-
153 7). The sediments from Ocean Drilling Program Hole 658C off Cap Blanc, Mauritania were
154 cored during ODP Leg 108 (Ruddiman et al., 1988).

155



156 **Figure 1.** Map showing studied core sites (white circles) and referenced core sites (black
 157 circles), JFM SSTs from the WOA18 (black contours; Locarnini et al., 2019), and ERA5 10m
 158 JFM winds (grey arrows; C3S, 2017). Studied core locations and water depths as follows: GC37
 159 (26°48.96'N, 15°7.06'W, 2771 m), GC49 (23°12.37'N, 17°51.25'W, 2303 m), ODP 658C
 160 (20°44.95'N, 18°34.85'W, 2263.6 m), GC68 (19°21.78'N, 17°16.94'W, 1396 m).

161

162 2.2 Age Models

163 The chronologies for the OC437-7 cores were developed from AMS radiocarbon ages on
 164 planktonic foraminifera (see Supplementary Information Figure S1). Radiocarbon ages younger
 165 than 20 ka in GC37 and GC68 and ages as old as 31.5 ka in GC49 were taken from McGee et al.
 166 (2013). Seven new radiocarbon ages were measured for this study (see Supplementary
 167 Information S1). The ages for this study were determined on specimens of *Globigerina*
 168 *bulloides*; radiocarbon measurements were performed at the Center for Accelerator Mass
 169 Spectrometry at Lawrence Livermore National Laboratory. Radiocarbon ages were converted to
 170 calendar ages using Marine13 (Reimer et al., 2013), with an additional reservoir correction (ΔR)

171 of 130 ± 50 yr (2σ) based upon local modern reservoir ages (Mulitza et al., 2010; Ndeye, 2008;
172 Pittauerov et al., 2009). We do not attempt to estimate past changes in reservoir age, though
173 these most certainly accompanied the dramatic changes in upwelling observed in African margin
174 records (Bradtmiller et al., 2016; Romero et al., 2008). Age models were interpolated between
175 ^{14}C tie points using the P_Sequence routine in OxCal 4.2 (Bronk Ramsey, 2008). This routine
176 provides Bayesian age-depth modeling and treats sediment deposition as a series of discrete
177 “events” following a Poisson distribution with a user-specified step size. A step size (k) of 0.75
178 cm^{-1} provided sufficient flexibility in the age-depth relationship to fit our ^{14}C ages.

179 The chronology for the ODP 658C core is based on AMS radiocarbon ages and
180 correlation to a geochemical record from a nearby core with existing age model (see
181 Supplementary Information Figure S2). From 20 ka to the coretop radiocarbon ages from
182 deMenocal et al. (2000) are utilized, and two new radiocarbon ages determined on specimens of
183 *Globigerina bulloides* were measured for this study to constrain the chronology from 38.5 to 30
184 ka. Radiocarbon ages were calibrated using Marine13 and a constant ΔR of 130 years. Between
185 67 ka and 25 ka the chronology is based on matching CaCO_3 weight percent in ODP 658C to
186 calibrated XRF CaCO_3 weight percent in neighboring core GeoB7920-2 (see Supplementary
187 Information Figure S3). The age model for this part of GeoB7920-2 is based on visual
188 correlation of the benthic (*Cibicidoides wuellerstorfi*) $\delta^{18}\text{O}$ record with that of marine sediment
189 core MD95-2042, with the $\delta^{18}\text{O}$ stratigraphy of MD95-2042 on the GRIP ss09sea age scale
190 (Tjallingii et al., 2008).

191

192 2.3 Determination of Biogenic Components and Aeolian Fraction of Sediments

193 The detrital percentage of the samples was calculated as the residual after subtracting the
194 carbonate, opal and organic carbon percentages measured at Macalester College. Percent
195 carbonate and percent total carbon were determined through coulometry. Percent organic carbon
196 was calculated as the difference between total carbon and carbonate carbon. Percent biogenic
197 opal was determined using alkaline extraction and molybdate blue spectrophotometry after the
198 method of Mortlock & Froelich (1989).

199 The aeolian fraction of the sediments was calculated by measuring grain size and
200 utilizing endmember modeling of grain size distributions to sum the two coarsest endmembers,
201 which are taken to represent the aeolian fraction of the detrital material, as determined above.

202 This approach derives from multiple studies showing that the grain size distributions of
203 northwest African margin can be approximated well by three endmembers (Holz et al., 2004,
204 2007; McGee et al., 2013; Mulitza et al., 2008; Tjallingii et al., 2008); that the two coarser
205 endmembers are similar in grain size to modern-day dust collected by dust traps (Stuut et al.,
206 2005); and that the finest endmember peaks in abundance near river mouths (Holz et al., 2004)
207 and varies in flux independently from the other two endmembers (McGee et al., 2013). Prior to
208 grain size measurement the non-detrital fraction of the sediment was removed in a stepwise
209 leaching procedure. Organic matter and calcium carbonate were removed in a glass beaker using
210 excess 10% hydrogen peroxide and 0.1 M hydrochloric acid, respectively. Opal was removed by
211 transferring the samples to centrifuge tubes, adding excess 2 M sodium carbonate, and heating
212 the samples in an 80°C hot bath for 5 hours. Grain size measurements were made on a Beckman
213 Coulter LS 13320 Laser Diffraction Particle Size Analyzer at the Royal Netherlands Institute for
214 Sea Research.

215 The grain size distribution below 250 μm was used for grain size endmember modelling
216 in order to separate aeolian from hemipelagic inputs. The grain size data for each core was fit
217 using Weibull distributions, which are unimodal, asymmetric distributions that closely
218 approximate measured grain size distributions of airborne dust and loess (Sun, 2004; Zobeck et
219 al., 1999). Three endmembers per core were used to model the grain size distributions, with the
220 two coarsest endmembers identified as aeolian dust, following the work of McGee et al. (2013).
221 The proportion of the grain size distribution that is accounted for by the two coarsest
222 endmembers was taken as the fraction of the detrital material that is aeolian, and this value was
223 multiplied by the detrital percentage to obtain the aeolian fraction of the bulk sediments.

224 The same endmember distributions that McGee et al., (2013) calculated for cores GC37,
225 GC49, and GC68 were utilized to estimate aeolian fractions for new sediment samples in this
226 study for those sites. For core ODP 658C best fit endmember distributions were calculated from
227 grain size distribution data on all samples analyzed in this study (from 67 to 18.8 ka), and used to
228 estimate the aeolian fraction of the bulk sediments (see Supplementary Information S3 and
229 Figure S4).

230

231 2.4 U, Th Isotope Measurements

232 Aeolian fluxes were calculated by multiplying the aeolian fraction of the sediments by
 233 the vertical sediment flux. Sediment fluxes were calculated using $^{230}\text{Th}_{\text{xs}}$ -normalization (Bacon,
 234 1984; Suman & Bacon, 1989), which utilizes the fact that the instantaneous ratio of water
 235 column scavenged ^{230}Th flux to the total sediment flux must be equal to the concentration of
 236 ^{230}Th in the underlying sediment:

$$\text{normalized aeolian flux} = \frac{\beta z}{[^{230}\text{Th}_{\text{xs}}^0]} F$$

238
 239 (Equation 1)

240
 241 where β is the production rate of ^{230}Th from ^{234}U in the water column (0.0268 dpm $\text{m}^{-3} \text{yr}^{-1}$,
 242 McGee et al., 2010), z is the water column depth (m), $[^{230}\text{Th}_{\text{xs}}^0]$ is the concentration of the
 243 component of the total $^{230}\text{Th}_{\text{meas}}$ that is not derived from detrital material or supported by ^{238}U
 244 decay within the sediments (in dpm/g), and has been corrected for decay since it was deposited,
 245 and F is the fraction of aeolian material. The water column depth was adjusted for changing sea
 246 level (Waelbroeck et al., 2002) as this affects the production rate of ^{230}Th in the water column.

247 $^{230}\text{Th}_{\text{xs}}^0$ is calculated using the following equation:

$$^{230}\text{Th}_{\text{xs}}^0 = e^{\lambda_{230}t} \times [^{230}\text{Th}_{\text{meas}} - ^{230}\text{Th}_{\text{det}} - ^{230}\text{Th}_{\text{auth}}]$$

249
 250 (Equation 2)

251
 252 The correction for decay was made using the age model of the core to assign an age to
 253 each sample and account for the decay of initial excess $^{230}\text{Th}_{\text{xs}}$ since the time of deposition. The
 254 detrital ^{230}Th was calculated by assuming the ^{232}Th content of the sample was entirely sourced
 255 from the detrital component, and calculating the activity of the ^{238}U associated with this detrital
 256 component using an estimated detrital $^{238}\text{U}/^{232}\text{Th}$ activity ratio of 0.7 ± 0.05 (1σ) for this area
 257 (Adkins et al., 2006). The detrital ^{230}Th is assumed to be in secular equilibrium with this
 258 uranium, so it can be subtracted from the $^{230}\text{Th}_{\text{meas}}$. Authigenic uranium is taken to be that which

259 remains after accounting for the detrital uranium. Authigenic ^{230}Th is therefore calculated by
260 assuming that the formation of authigenic minerals/coatings occurs at the time of sediment
261 deposition and incorporates $^{234}\text{U}/^{238}\text{U}$ at a constant seawater activity ratio of 1.1468 (Andersen et
262 al., 2010).

263 In preparation for isotopic measurements samples were weighed, doped with a mixed
264 spike of ^{229}Th and ^{236}U , and fully dissolved with hydrogen peroxide, nitric acid, hydrochloric
265 acid and hydrofluoric acid. An iron coprecipitation step allowed removal of much of the matrix
266 of the dissolved sediments and thus improved yields of Th and U. Samples then underwent anion
267 exchange chromatography using Dowex Bio-Rad AG1-X8 100-200 mesh anion exchange resin
268 to separate Th and U so that the two elements could be measured separately. ^{230}Th , ^{232}Th , and
269 ^{238}U isotope measurements were made using a multi-collector inductively coupled plasma source
270 mass spectrometer (MC-ICP-MS). The majority of isotopic measurements were made using a
271 ThermoScientific Neptune Plus MC-ICP-MS at Brown University; more recent measurements
272 were made on a Nu Plasma II-ES MC-ICP-MS at MIT.

273 Uncertainties in the final aeolian fluxes reported reflect confidence limits associated with
274 mass spectrometric measurements, the detrital U/Th ratio, and the aeolian fraction of the
275 sediments. The uncertainties in aeolian fluxes do not incorporate uncertainties in the assumption
276 that the supply of scavenged ^{230}Th to the sediment is equivalent to the production rate of ^{230}Th in
277 the overlying water column. Our core sites lie in an exceptionally productive region of upwelling
278 which can lead to boundary scavenging of ^{230}Th : there is strong year round upwelling from 20 to
279 26°N along the West African margin, with weaker year round upwelling north of 26°N , and
280 seasonal upwelling south of 20°N (Gómez-Letona et al., 2017). Currently, boundary scavenging
281 of ^{230}Th has been constrained to $40 \pm 10\%$ of its water column production off northwest Africa
282 (Hayes et al., 2015), helping to quantify this additional uncertainty associated with ^{230}Th -
283 normalized sediment fluxes in our study region. This scavenging would increase ^{230}Th deposition
284 in sediments at our core sites, biasing our accumulation rates low. It is assumed that changes in
285 anomalous ^{230}Th deposition due to changes in boundary scavenging are much smaller than the
286 factor of >3 changes in aeolian flux seen in our records, meaning that relative changes in flux are
287 likely to be robust even if the mean flux is biased low.

288 **3 Results**

289 The meridional sediment core transect along the northwest African margin reveals
290 latitudinal differences in the relative expressions of low-latitude (orbital monsoon) and high-
291 latitude (glacial and stadial event) forcing on regional dust fluxes and coastal upwelling (Figure
292 2). Dust, opal, and organic carbon fluxes for the 20 ka to coretop portions of GC37, GC49 and
293 GC68 were previously published in McGee et al., (2013) and Bradtmiller et al., (2016),
294 respectively. Carbonate, opal, and detrital fluxes for the 20 ka to coretop portion of ODP 658C
295 were previously published in Adkins et al., (2006).

296

297 3.1 GC37 (27°N)

298 Dust fluxes in core GC37 exhibit a maximum from 36 to 31 ka during late marine isotope
299 stage (MIS) 3 ($\sim 0.5 \text{ g cm}^{-2} \text{ kyr}^{-1}$), with a millennial-scale peak coincident with H3 (31.3 ka)
300 (Sánchez Goñi & Harrison, 2010). Fluxes gradually fall during MIS 2 to moderately low values
301 ($0.26 \text{ g cm}^{-2} \text{ kyr}^{-1}$) in the late LGM (~ 20 ka), with a small dust peak associated with H2 (24 ka).
302 Dust fluxes rise to millennial-scale peaks during H1 ($0.37 \text{ g cm}^{-2} \text{ kyr}^{-1}$) and the YD (0.47 g cm^{-2}
303 kyr^{-1}), with the YD showing a 20% higher peak flux of dust than H1. Fluxes abruptly fall during
304 the onset of the AHP at ~ 12 ka, and continue to fall to the lowest recorded value at ~ 6 ka (0.09
305 $\text{g cm}^{-2} \text{ kyr}^{-1}$). Dust fluxes then increase into the Late Holocene (~ 1 ka) to a value of $\sim 0.2 \text{ g cm}^{-2}$
306 kyr^{-1} .

307 Both opal and organic carbon fluxes are highly correlated with dust fluxes in core GC37
308 ($r^2 = 0.69$; $p\text{-value} < 0.05$ and $r^2 = 0.43$; $p\text{-value} < 0.05$, respectively). Similar to dust, both opal
309 and organic carbon are at maximum levels at ~ 36 ka, the base of the core. Biogenic fluxes
310 decrease into the LGM, with opal more closely tracking dust and organic carbon dropping
311 rapidly after 30 ka. Opal fluxes rise to high levels during both H1 and the YD, while organic
312 carbon fluxes peak only in H1. Fluxes of both opal and organic carbon fall to low levels
313 throughout the AHP before rising during the late Holocene.

314

315 3.2 GC49 (23°N)

316 Dust fluxes in core GC49 decrease steadily from a late MIS 3 maximum at 36 ka (0.74 g
317 $\text{cm}^{-2} \text{ kyr}^{-1}$) to moderately low values during the late LGM at ~ 21 ka ($0.52 \text{ g cm}^{-2} \text{ kyr}^{-1}$), with a
318 small peak coincident with H2 (24 ka). Dust fluxes then rise to peaks during H1 ($0.65 \text{ g cm}^{-2} \text{ kyr}^{-1}$)

319 ¹) and the YD (0.84 g cm⁻² kyr⁻¹), before decreasing to a minimum during the AHP (0.076-0.11 g
320 cm⁻² kyr⁻¹). Similar to the GC37 record, the dust flux peak associated with the YD is larger – by
321 ~30% – than the H1 peak, showing a stronger dust response during the YD in the northern core
322 sites. Dust fluxes then increase into the Late Holocene to a value of 0.52 g cm⁻² kyr⁻¹.

323 Both opal and organic carbon fluxes are highly correlated with dust fluxes in core GC49
324 ($r^2 = 0.45$; p-value < 0.05 and $r^2 = 0.39$; p-value < 0.05, respectively). Opal and organic carbon
325 fluxes are at high levels during late MIS 3 at ~36 ka, the end of the core, and both decrease into
326 the LGM. Opal fluxes more closely track dust fluxes, also showing a peak coincident with H2
327 (24 ka), while the organic carbon fluxes drop rapidly after 30 ka and are highly variable during
328 the early part of the LGM. Opal fluxes rise to high levels during H1 and the YD, while organic
329 carbon fluxes peak only in H1 and show an earlier peak from 21-18 ka at the end of the LGM.
330 Fluxes of both opal and organic carbon fall to low levels throughout the AHP before rising
331 during the late Holocene.

332

333 3.3 GC68 (19°N)

334 Core GC68 provides the highest resolution dust fluxes in this study due to the high
335 sediment accumulation rates at this site, which is the closest site in the transect to the core of the
336 Saharan dust plume. The highest sedimentation rates are in the older portion of the core, from 26
337 to 13 ka, at a time when the dust fraction of the material averages 80 to 90 %, meaning that we
338 can dismiss other inputs, such as nearby paleorivers, as a major component of material at this site
339 (Drake et al., 2010; Skonieczny et al., 2015). From 26 ka to the end of the LGM, dust fluxes
340 show a slight decrease punctuated by abrupt rises and falls between values of ~4.5 to ~2 g cm⁻²
341 kyr⁻¹, including a small peak coincident with H2 (24 ka) and a prominent peak at ~21 ka. Dust
342 fluxes then rise to peaks during H1 (~6 g cm⁻² kyr⁻¹) and the YD (~4.2 g cm⁻² kyr⁻¹), before
343 decreasing to a minimum during the AHP (0.39-0.49 g cm⁻² kyr⁻¹). In contrast to cores GC37 and
344 GC49, the H1 peak dust flux is larger than the YD peak dust flux (by ~50%), showing a stronger
345 dust response during H1 at this southern core site. Dust fluxes then increase into the Late
346 Holocene (~2 ka) to a value of 1.64 g cm⁻² kyr⁻¹.

347 Opal fluxes are highly correlated with dust fluxes in core GC68 ($r^2 = 0.44$; p-value <
348 0.05), while organic carbon fluxes show very low correlation ($r^2 = 0.02$; p-value > 0.05). From
349 26 ka, the end of the core, to the end of the LGM opal fluxes show a slight decrease punctuated

350 by abrupt rises and falls similar to the dust record, also recording peaks coincident with H2 and
351 at ~21 ka. Organic carbon fluxes show a substantial difference from dust fluxes from 26 ka to the
352 end of the LGM with no noticeable trend and high variability. Biogenic fluxes rise to high levels
353 during both H1 and the YD, with the YD peak slightly larger than the H1 peak in both opal and
354 organic carbon fluxes. Fluxes of both opal and organic carbon fall to low levels throughout the
355 AHP before rising during the late Holocene.

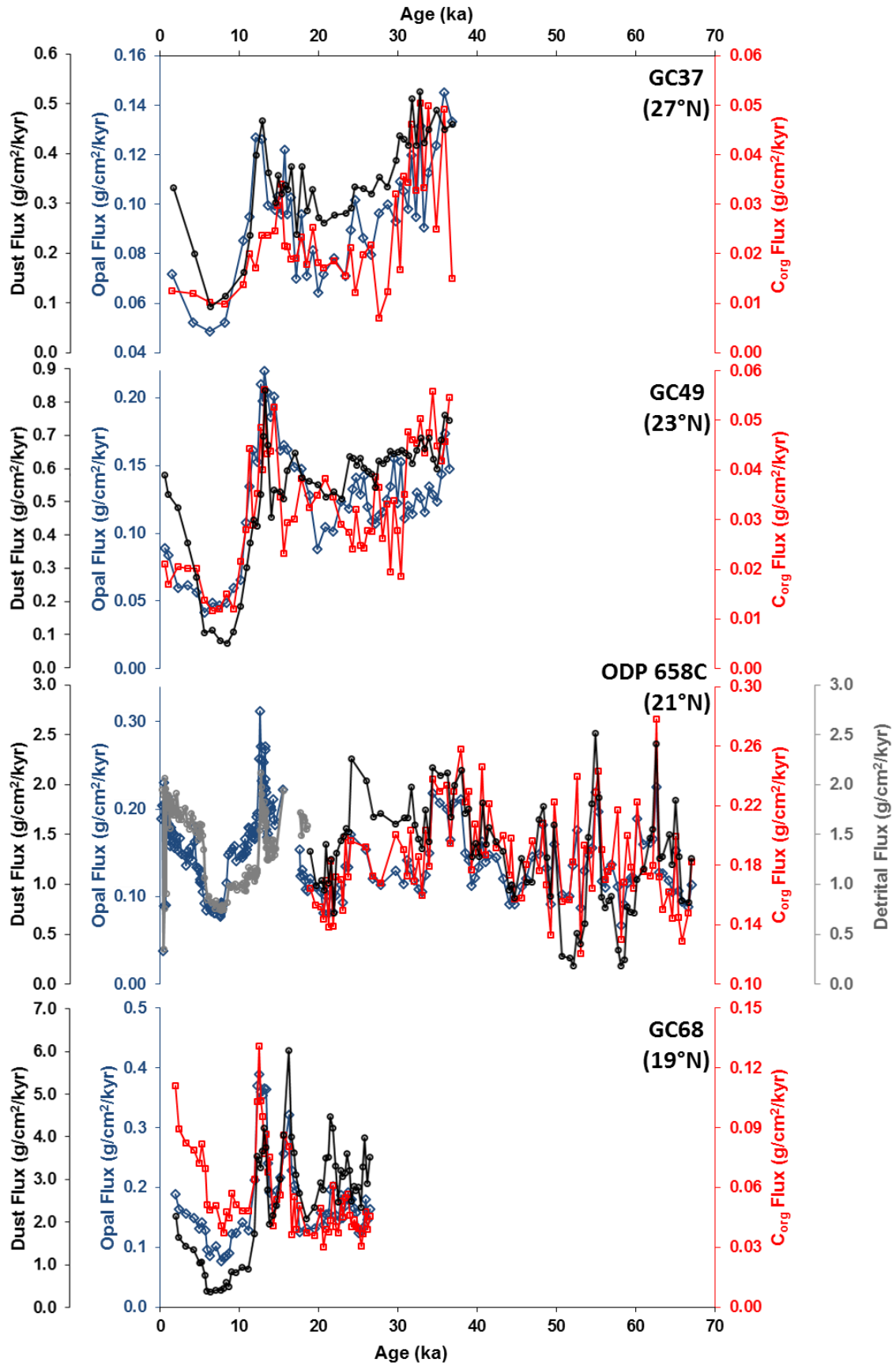
356

357 3.4 ODP 658C (21°N)

358 The ODP 658C core provides a longer archive than the CHEETA cores and allows
359 continued high-resolution study of dust accumulation rates to the margin. Here we extend the
360 record back to 67 ka. The early portion of the record at the latter stages of MIS 4 shows moderate
361 dust fluxes to the margin followed by an abrupt peak ($2.4 \text{ g cm}^{-2} \text{ kyr}^{-1}$) coincident with H6 (62.5
362 ka). This is followed by a decline in dust flux over 3 ka to an interval from 60-50 ka when the
363 lowest dust fluxes ($0.18 \text{ g cm}^{-2} \text{ kyr}^{-1}$) observed in the record for this site are recorded. This low
364 dust interval is interrupted by an abrupt (millennial-scale) dust increase to the highest fluxes (2.5
365 $\text{g cm}^{-2} \text{ kyr}^{-1}$) observed in the whole record centered at H5a (55 ka). A trend of increasing
366 dustiness is then observed after the end of the 60-50 ka low dust interval, reaching a maximum
367 ($\sim 2.1 \text{ g cm}^{-2} \text{ kyr}^{-1}$) at 35 to 33 ka. Millennial-scale variability is superimposed on this broad
368 trend, including a peak in flux ($1.8 \text{ g cm}^{-2} \text{ kyr}^{-1}$) coincident with H5 (48 ka). Dust fluxes decrease
369 from the late MIS 3 maximum to $\sim 1 \text{ g cm}^{-2} \text{ kyr}^{-1}$ at the end of the LGM (20 ka), with millennial-
370 scale abrupt peaks in flux of $2 \text{ g cm}^{-2} \text{ kyr}^{-1}$ and $2.26 \text{ g cm}^{-2} \text{ kyr}^{-1}$, coincident with H3 (31.3 ka)
371 and H2 (24 ka) respectively. Following the LGM, the remainder of the dust record from this site
372 is a detrital flux record (Adkins et al., 2006), as grain size-based estimates of the aeolian fraction
373 of detrital sediments are not available. Detrital fluxes rise to millennial-scale peaks during H1
374 ($1.94 \text{ g cm}^{-2} \text{ kyr}^{-1}$) and the YD ($2.12 \text{ g cm}^{-2} \text{ kyr}^{-1}$) before decreasing to sustained low values
375 ($0.75\text{-}1 \text{ g cm}^{-2} \text{ kyr}^{-1}$) during the AHP; a hiatus occurs during H1, so the peak of H1 fluxes is
376 missing in this record. Detrital fluxes increase abruptly at 5 ka and continue to rise steadily into
377 the Late Holocene to a value of $\sim 2 \text{ g cm}^{-2} \text{ kyr}^{-1}$.

378 Both opal and organic carbon fluxes are positively correlated with dust fluxes in core
379 ODP 658C ($r^2 = 0.46$; p-value < 0.05 and $r^2 = 0.32$; p-value < 0.05 , respectively). Both opal and
380 organic carbon fluxes increase from moderate values at the end of MIS 4 to two peaks coincident

381 with H6 and H5a separated by an interval of lower fluxes, with the organic carbon showing
382 higher amplitude rises and falls during the interval of lower fluxes. Biogenic fluxes variably rise
383 and fall from H5a until ~45 ka when both opal and organic carbon fluxes gradually increase to a
384 maximum at 38 to 34 ka. Both opal and organic carbon fluxes drop sharply at 33 ka and remain
385 low throughout MIS 2 and the LGM, with small peaks at H3 and H2. The opal flux record shows
386 peaks during H1 and the YD, falls to low levels throughout the AHP, and rises during the late
387 Holocene. From the end of the LGM to the Holocene organic carbon concentrations have not
388 been measured.



390 **Figure 2.** Opal (blue line, open diamonds), C_{org} (red line, open squares), dust (black line, open
391 circles), and detrital (grey line, open circles) flux records arranged from north to south as labeled.
392 Data <20 ka in GC37, GC49, and GC68 from Bradtmiller et al., (2016); data <20 ka in ODP
393 658C from Adkins et al., (2006).

394

395 **4 Discussion**

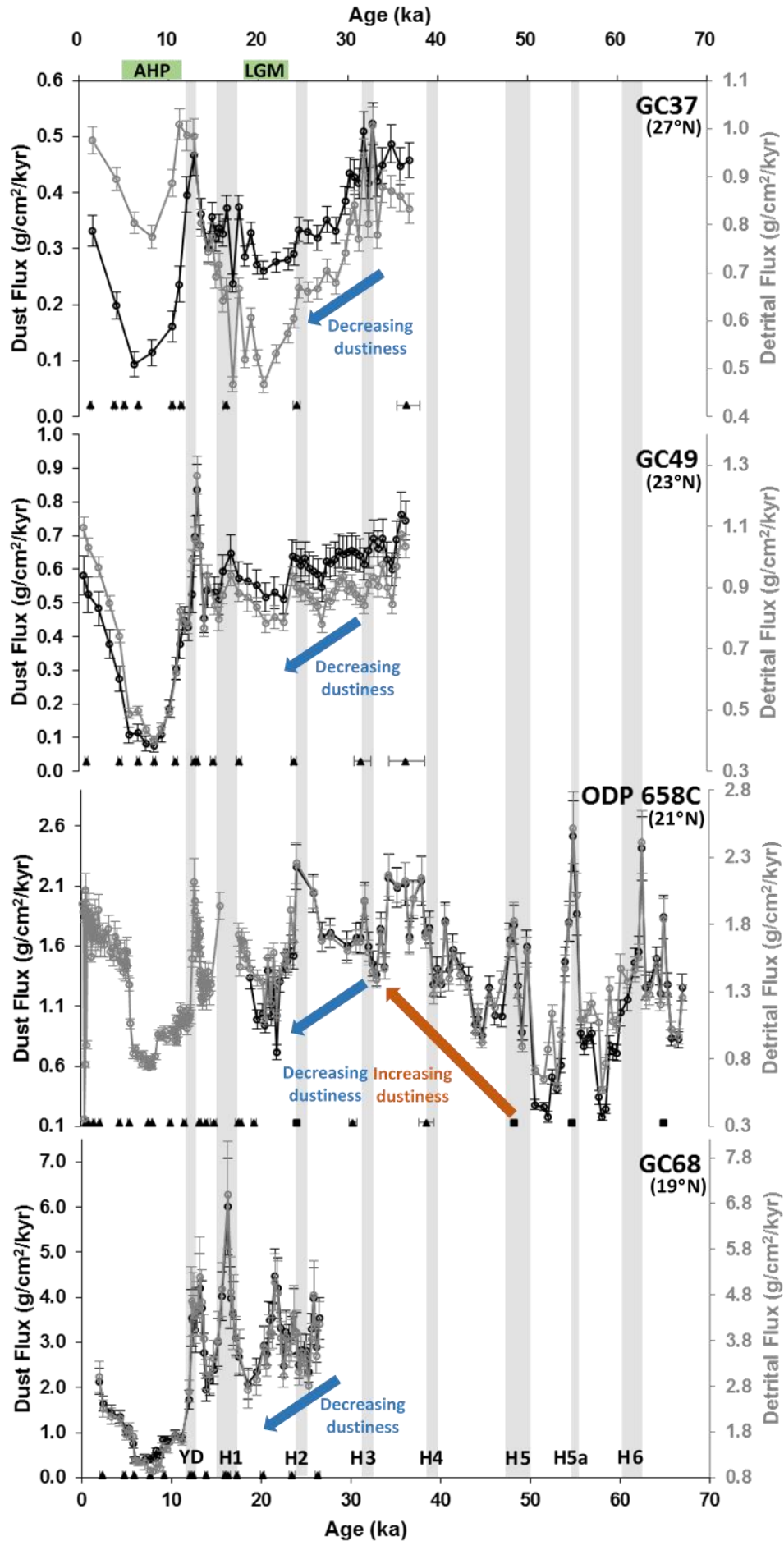
396 4.1 Coherence of African Margin and Mid-Atlantic Dust Flux Records

397 This work has extended the CHEETA dust flux records to the bottom of cored material
398 reaching back to 37 ka in GC37, 36.5 ka in GC49, and 26.5 ka in GC68, and produced a dust
399 flux record from 67 to 19 ka for the core from ODP Hole 658C (Figure 3). The extended portions
400 of the ODP 658C, GC37, and GC49 records overlap from 37 ka to 20 ka and demonstrate
401 coherent variation on both orbital and millennial timescales. In ODP 658C, Heinrich events 2
402 and 3 are recorded as increases in dust flux superimposed on a decreasing trend of dustiness
403 through the end of the LGM. The GC68 record also shows H2 recorded as a time of increased
404 dust flux, and a decreasing trend of dustiness through the end of the LGM, while also showing
405 higher frequency variability from 26 to 20 ka with multiple abrupt peaks in dust flux. In the
406 northern core sites (ODP 658C through GC37, 21°-27°N), peak dust fluxes in early MIS 2 (27 to
407 23 ka) are similar to modern, and only in the southernmost core site (GC68, 19°N) are early MIS
408 2 fluxes higher than modern (by ~50%). In all cores, dust fluxes drop from early MIS 2 to the
409 LGM (23 to 19 ka) by 20-40%. The strong agreement between dust records from 37 to 19 ka
410 gives us confidence that the extended ODP 658C record from 67 to 37 ka is faithfully recording
411 the export of dust to the margin.

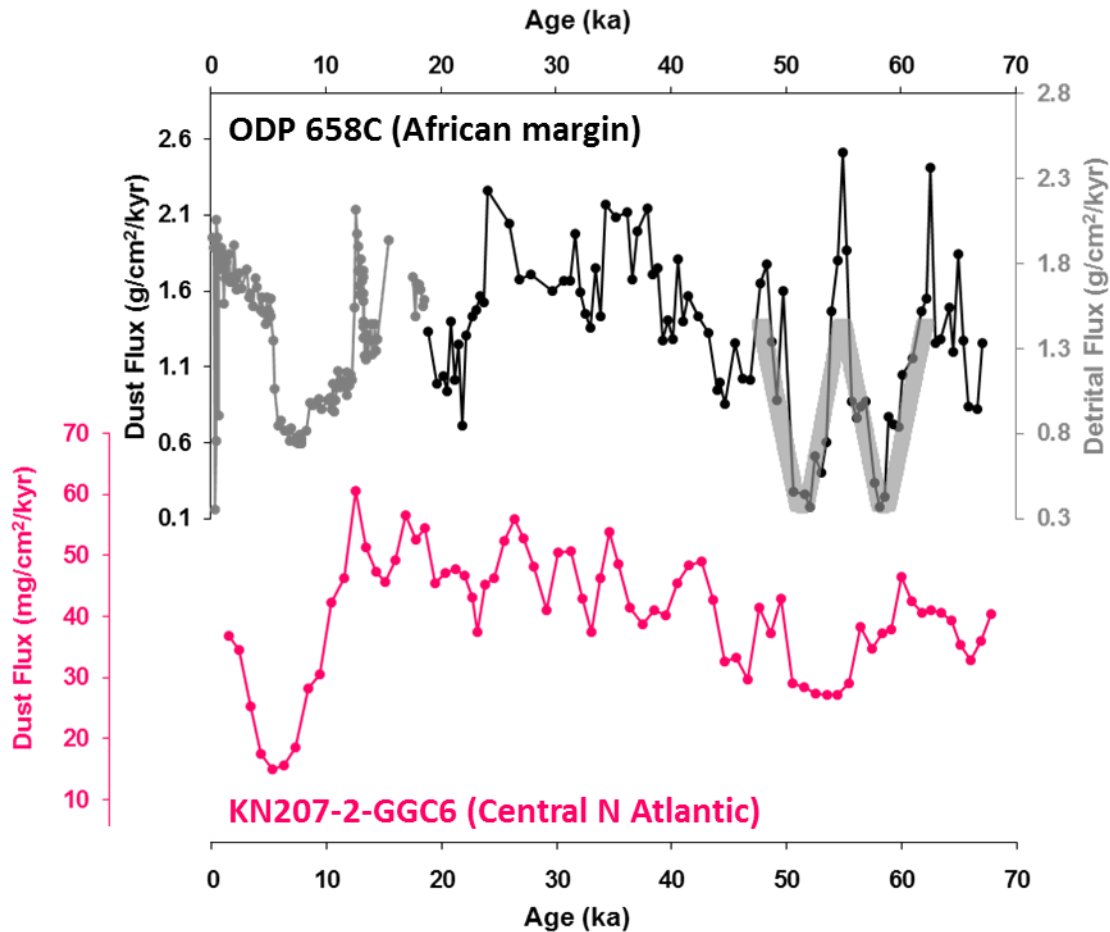
412 The ODP 658C record shows remarkable similarity to the dust flux record covering the
413 last 70 ka from the Mid-Atlantic at 25°N (Middleton et al., 2018), both in overall trends and
414 millennial-scale variability (Figure 4). Both records exhibit a background increase in dustiness
415 throughout MIS 3, a large decrease during the AHP, and peaks in dust flux during Greenland
416 stadials. There are two distinct times of disagreement between the records, namely during the
417 AHP through the late Holocene, and from 60 to 50 ka. In the Mid-Atlantic record, the AHP has a
418 more gradual onset and ends 2 ka later than in the ODP 658C record. From 60 to 50 ka the ODP
419 658C record exhibits much higher variability with fluxes reaching both their maximum and
420 minimum levels of the whole 67 ka record. These disagreements are likely a consequence of low

421 sedimentation rates at the Mid-Atlantic site (averaging 2 cm/kyr), whereas the ODP 658C site
422 has an average sedimentation rate of 16 cm/kyr. The high amplitude and abrupt changes in dust
423 flux during the AHP and the 60 to 50 ka humid period are well resolved due to the high
424 sedimentation rates at the ODP 658C site (Figure 4), whereas the amplitude of these abrupt
425 changes may have been smoothed due to the much lower sedimentation rate and thus greater
426 influence of mixing by bioturbation at the Mid-Atlantic site.

427 The agreement with the Mid-Atlantic dust record, which lies thousands of miles
428 downwind of African dust sources, is important in that the site is likely to be biased toward
429 summer rather than winter dust emissions, and it presumably reflects dust from a wider region of
430 North Africa than the margin sites. Consistent with previous work (Williams et al., 2016), this
431 comparison suggests that the summer and winter dust plumes, and dust deposition at both
432 proximal and distal sites, have largely varied in sync over the late Pleistocene. The agreement
433 also builds confidence that the variations in sea-level (and thus in the distance to dust source
434 areas) has not had a substantial influence on dust deposition at the margin sites. Therefore, the
435 ODP 658C dust record appears to be representative of an integrated signal of African dust export
436 to the North Atlantic over the past 67 ka.



438 **Figure 3.** Dust (black line, open circles) and detrital (grey line, open circles) flux records
 439 arranged from north to south as labeled with 1σ uncertainties shown. Data <20 ka in GC37,
 440 GC49, and GC68 from McGee et al., (2013), data <20 ka in ODP 658C from Adkins et al.,
 441 (2006). ^{14}C tie points and 1σ uncertainties shown as black triangles, CaCO_3 tie points for ODP



442 658C shown as black squares.

443 **Figure 4.** ODP 658C dust and detrital flux records (black and grey lines, respectively) and
 444 KN207-2-GGC6 dust flux record from the mid-Atlantic (Middleton et al., 2018) (pink line). Data
 445 <20 ka in ODP 658C from Adkins et al., (2006). “W-shape” structure of the dust flux record as
 446 referred to in main text is illustrated by a transparent grey w-shape from ~60 to 50 ka.

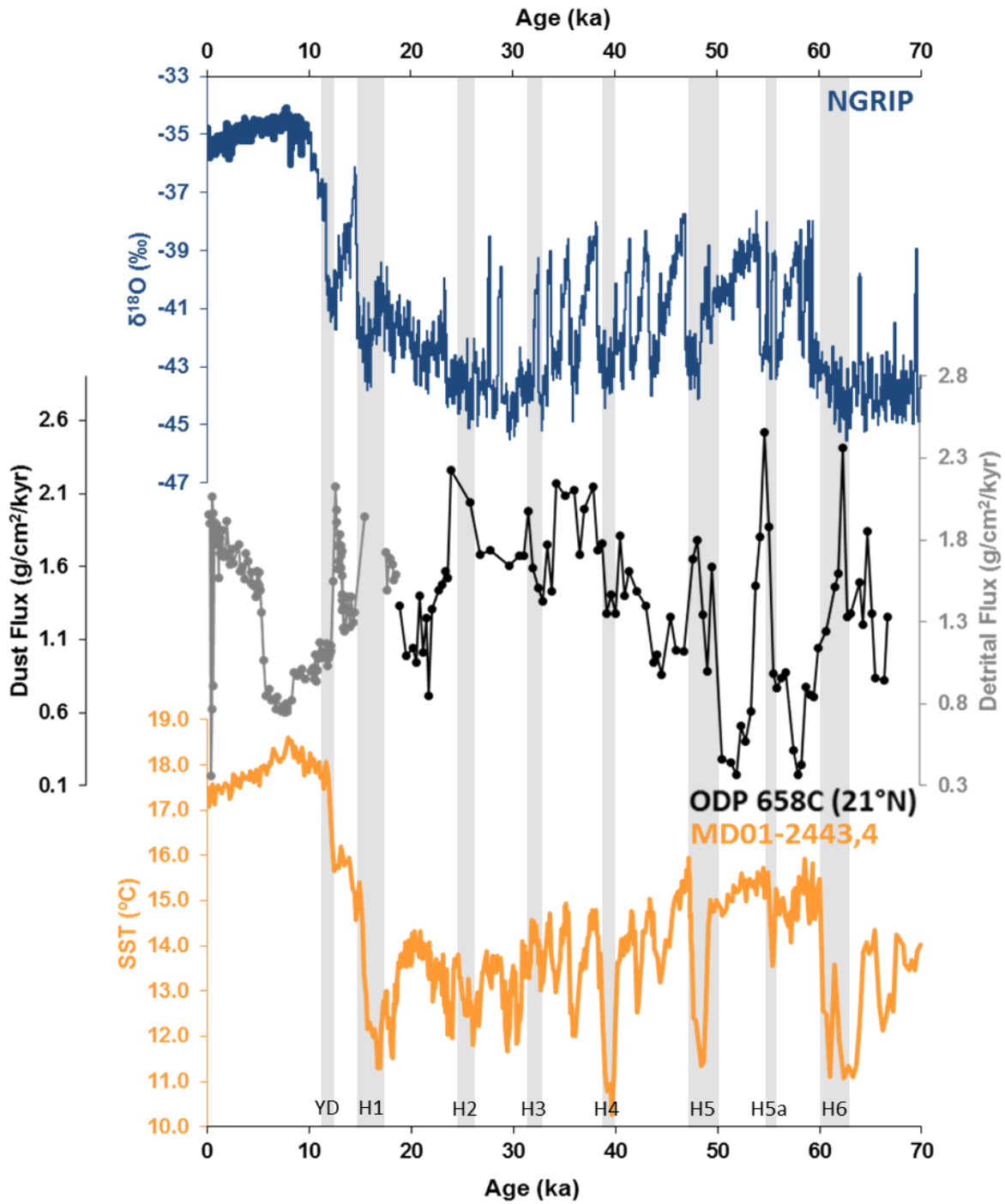
447

448 4.2 Major Features of Dust Flux Records from 67 to 20 ka (MIS 4 through 2)

449 We begin by describing the broader-scale features of the records before turning to
 450 millennial-scale variability. At the onset of MIS 3 (~60 ka) Northern Hemisphere temperatures

451 increase, and during this time dust fluxes in ODP 658C drop to values comparable to those
452 during the AHP (a direct comparison of dust fluxes is not possible because Adkins et al. (2006)
453 reported total detrital fluxes, providing only an upper bound on dust fluxes). Over the next 30 ka,
454 Northern Hemisphere high-latitude temperatures reflected in Greenland ice core records decrease
455 gradually to minimum values between 30 and 25 ka, with multiple millennial-scale stadials
456 superimposed on the background decrease (Figure 5; colder temperatures are oriented upwards)
457 (Seierstad et al., 2014). Dust fluxes over this interval show a gradual increase to sustained high
458 values during the end of MIS 3 and early MIS 2, with millennial-scale pulses of high dust flux
459 superimposed on the background increase.

460 During MIS 2, Northern Hemisphere high-latitude temperatures gradually increase after
461 24 ka leading into the LGM time slice commonly targeted for data-model comparisons (23 to 19
462 ka) (e.g., Waelbroeck et al., 2009). Dust fluxes over this interval decrease from the high values
463 observed at 30 to 25 ka; as a result, in all but the southernmost core (GC68, 19°N) the LGM is
464 characterized by dust deposition rates that are similar to late Holocene fluxes. The broad scale
465 features of the dust records from the end of MIS 4 through the end of MIS 2 show a strong
466 correspondence over this interval between high latitude temperatures and dust fluxes to the
467 margin, with lower temperatures associated with higher fluxes to the margin and higher
468 temperatures associated with lower fluxes to the margin.

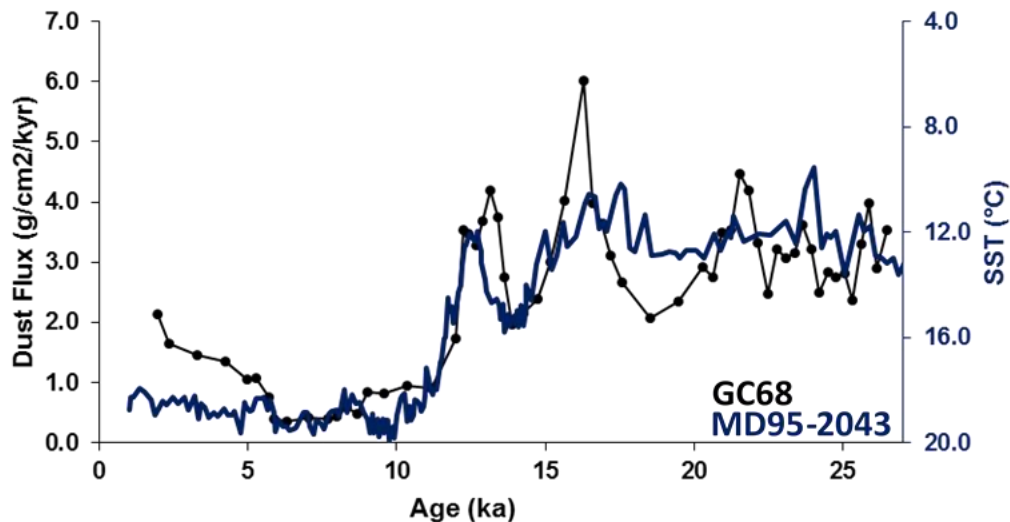


469

470 **Figure 5.** NGRIP $\delta^{18}\text{O}$ from Seierstad et al., (2014) (blue line), ODP 658C dust and detrital flux
 471 records (black and grey lines, respectively), and MD01-2443,4 SST record from Martrat et al.,
 472 (2007) (orange line). Data <20 ka in ODP 658C from Adkins et al., (2006).

473

474 The high sedimentation rates and well-resolved radiocarbon-based age model for GC68
 475 allows a more detailed comparison between dust flux variability and millennial-scale high
 476 latitude climate records over the last 26 ka. The millennial-scale features in the GC68 dust flux
 477 record associated with high-latitude climate fluctuations during H1, the Bølling-Allerød warm
 478 period, and the YD, previously described by McGee et al., (2013), show strong coherence
 479 between North Atlantic stadials and high fluxes of dust to the West African margin. Comparison
 480 of the earlier highly-resolved 26.5 to 20 ka portion of the GC68 flux record (Figure 6) with a
 481 proxy record of North Atlantic SSTs (Cacho et al., 1999) reveals that the three cold events at 25
 482 ka, 24 ka (H2) and 21 ka are all associated with increases of dust flux to the margin. The
 483 amplitudes of dust flux over this interval do not have a clear correspondence with amplitude of
 484 SST (i.e. the largest dust flux peak does not occur at the time of coldest SST), which could be
 485 caused by variable bioturbation and smoothing of the peaks in the two records.



486
 487 **Figure 6.** GC68 dust flux record (black line) and MD95-2043 SST record from Cacho et al.,
 488 (1999) (blue line). Data <20 ka in GC68 from McGee et al., (2013).

489
 490 While the GC68 cored material ends at 26.5 ka, the older material from CHEETA cores
 491 GC37 and GC49 and ODP Core 658C shows peaks of dust flux likely associated with earlier
 492 millennial-scale North Atlantic stadial events. At 62.5 ka there is a pronounced stadial (including
 493 Heinrich event 6) in the North Atlantic with an accompanying millennial-scale peak in which

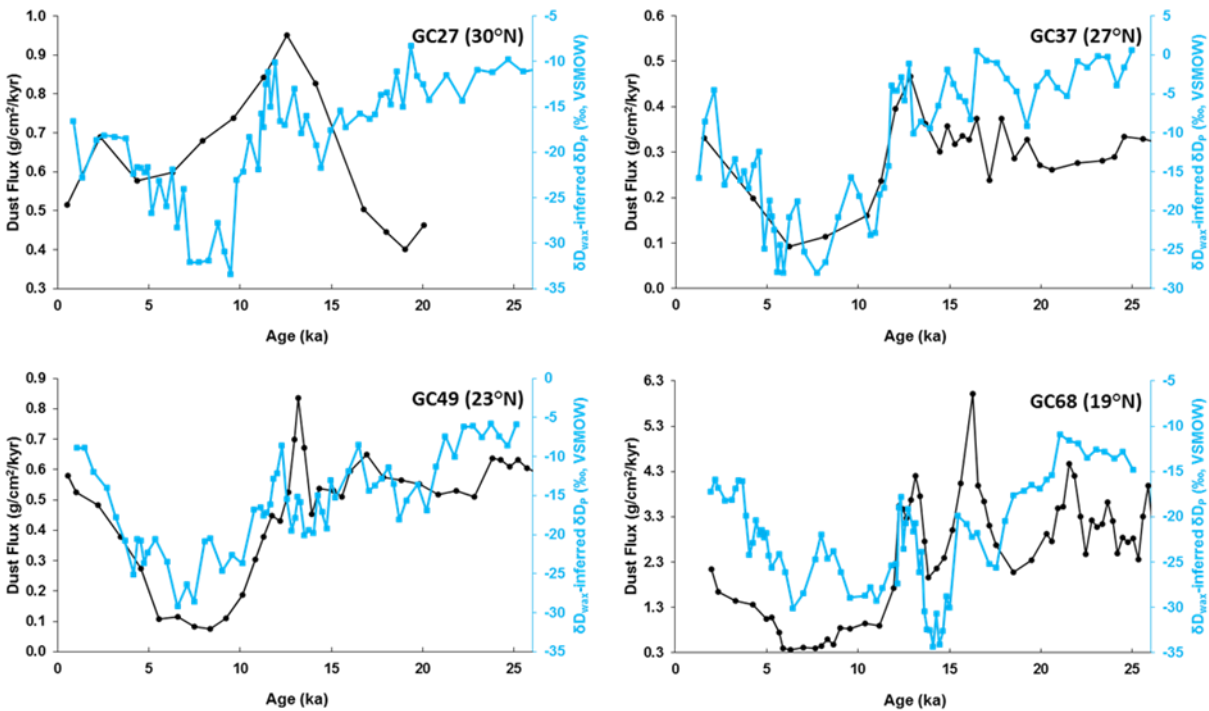
494 dust fluxes at ODP 658C more than double. This signal of increased dust during stadials with
495 associated Heinrich events is a robust response, with dust increases seen at H5a, H5, H3, and H2.
496 The exception to this is H4 which occurs at a time in ODP 658C where dust is at a minimum; we
497 suggest that this mismatch is due to age model error (see Supplementary Information S1), and
498 that the subsequent dust flux peak is a response to H4. A similar mismatch is evident in the mid-
499 Atlantic record of Middleton et al. (2018). There are also stadial events (without accompanying
500 H events) with pronounced dust flux peaks at 42 ka and 37 ka, showing that increased export of
501 dust is observed during stadials both with and without H events. There are multiple instances in
502 which stadials are observed in the SST record without discernible increases in dust flux (67 ka,
503 47 ka, 30 ka), perhaps due to aforementioned age model error, or increased smoothing by
504 bioturbation during times of lower sedimentation rates (see Supplementary Information S2).

505 Based upon the strong coherence between millennial-scale peaks in dust flux in our most
506 robust record (GC68) with stadials in the North Atlantic, we suggest that the millennial-scale
507 peaks in the longer dust flux records (ODP 658C, GC49, GC37) correspond to the millennial-
508 scale stadial events in the North Atlantic SST records, and that any mismatches are likely due to
509 issues with smoothing and age control. This conclusion, which could be strengthened by
510 additional records with consistently high accumulation rates as in CHEETA core GC68, suggests
511 that the impact of Heinrich events on West African climate was largely stable across varying
512 orbital configurations and ice sheet extents during MIS 2, 3, and 4.

513

514 4.3 Implications for Wind and Precipitation Changes over North Africa During North 515 Atlantic Cooling Events

516 These new data, in combination with previously published records, provide a clear
517 picture of climate changes in stadial times in North Africa. First, it is clear that stadials are
518 marked by both precipitation decreases and strengthening of northeasterly winds over North
519 Africa. Stadials are marked by reduced precipitation in the Sahel and a southward shift of the
520 Sahel/Sahara boundary (Collins et al., 2013; Weldeab et al., 2007). In the Sahara, leaf wax δD
521 data from the CHEETA cores spanning the last 25 ka also document dry conditions in northwest
522 Africa during stadial events (Tierney et al., 2017). However, northwest African margin δD
523 values are no more positive during stadials than in the late Holocene (Figure 7), perhaps because
524 precipitation cannot decrease much more than its current levels in the Sahara.



525

526

527 **Figure 7.** Dust flux records (black line) and δD_{wax} -inferred hydrogen isotopic composition of
 528 precipitation records (δD_{p}) (blue line; Tierney et al., 2017) at CHEETA sites GC27, GC37,
 529 GC49, and GC68 as labeled (black lines). Data <20 ka in GC27, GC37, GC49, and GC68 from
 530 McGee et al., (2013).

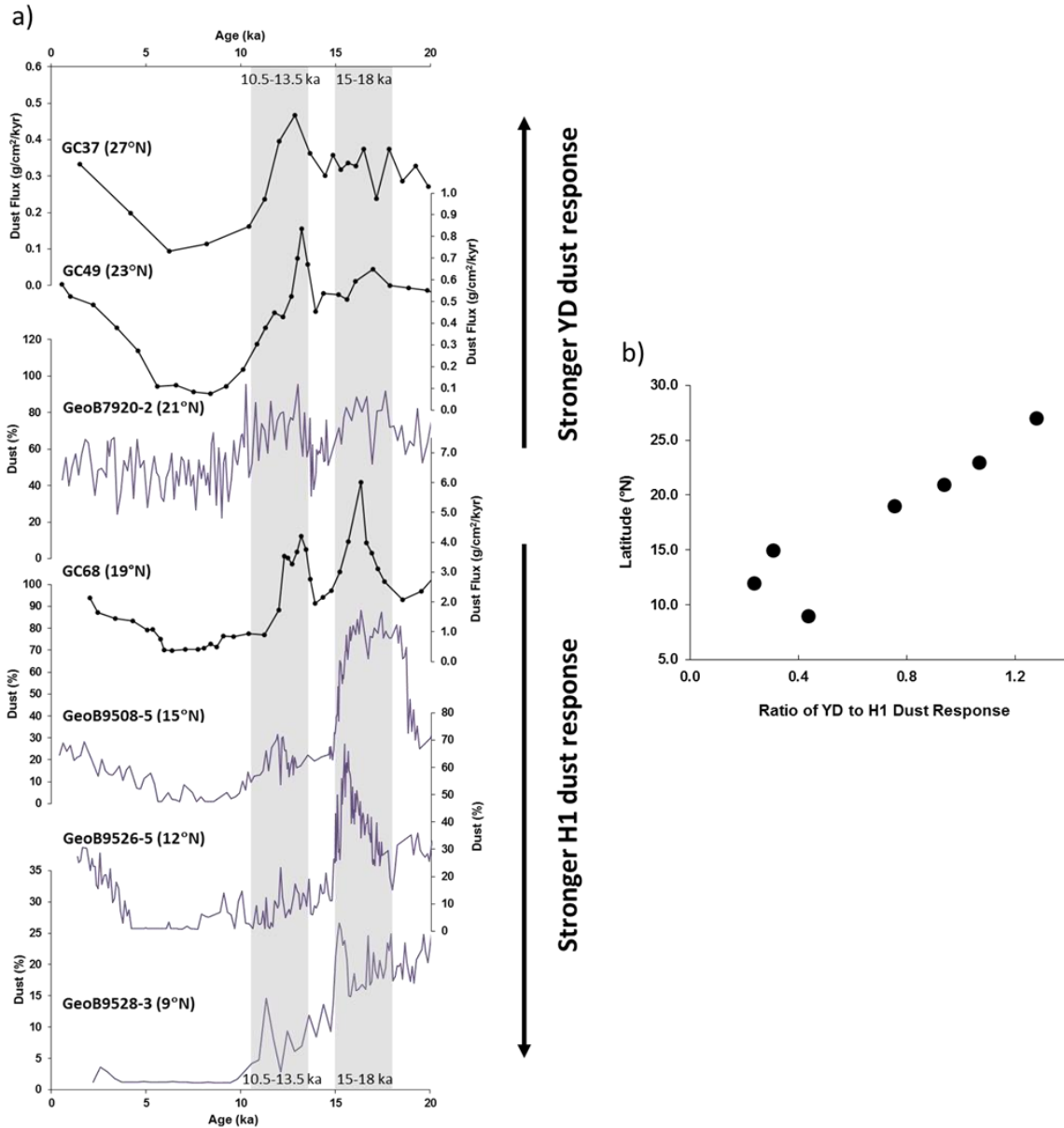
531

532 For the Saharan dust sources relevant for the northwest African margin and central
 533 Atlantic cores, increased aridity is thus unlikely to explain dust fluxes roughly double late
 534 Holocene values during stadials. Instead, Murphy et al. (2014) suggest that in areas that are
 535 already dry and dust producing like the Sahara, the only way to increase dust export is through
 536 an increase in wind speed; this conclusion is supported by studies supporting the dominant role
 537 of winds in modern decadal variability in Saharan dust emissions (Ridley et al., 2014; Wang et
 538 al., 2015). Consistent with this conclusion, our records show strong covariation of opal and
 539 organic carbon fluxes with dust fluxes throughout most of our records (Figure 7), providing firm
 540 evidence for intensification of northeasterly winds as a driver of increases in both coastal
 541 upwelling and dust deposition during stadials (Bradtmitter et al., 2016; McGee et al., 2018).

542 Another potential mechanism which could explain the covariation is ballasting of organic
543 material by dust particles. This has been shown to occur off Mauritania with Saharan dust
544 ballasting organic matter (van der Jagt et al., 2018), potentially increasing export by an order of
545 magnitude, however this mechanism is unlikely to explain the covariation of opal fluxes with
546 dust export.

547 A modeling study by Liu et al. (2014) highlights the importance of these wind anomalies
548 in communicating stadial conditions to the West African monsoon, demonstrating that
549 anomalous northeasterly winds resulting from high-latitude cooling advect cold, dry air into
550 North Africa, weakening the west African monsoonal circulation and drying the Sahel. This cold
551 air advection is amplified by water vapor feedbacks, which further cool the Sahara and raise
552 surface pressures, increasing northeasterly winds even more (Liu et al., 2014). Our dust and
553 biogenic flux records thus provide support for Liu et al.'s ventilation mechanism as a driver of
554 the reductions in Sahel rainfall suggested by proxy data during stadials (e.g., Weldeab et al.,
555 2007). In stadials, as in modern decadal-scale variability (Wang et al., 2015), reduced Sahel
556 precipitation occurs in association with strengthened northeasterly winds over the Sahara.

557 Combining West African margin dust flux and dust percentage data to form a north-south
558 transect (Figure 8a), we also observe important latitudinal differences in the wind anomalies
559 associated with different stadial events. These differences are most robust during H1 and the YD,
560 periods for which dating uncertainties are relatively small and the most records exist. In records
561 south of 20°N, dust increases during H1 are especially prominent, while dust changes during the
562 YD relatively muted. The opposite is true north of 20°N, as the YD dust flux peak is
563 substantially greater than the H1 peak at 23°N and 27°N. Figure 8b shows a consistent increase
564 in the YD:H1 dust flux ratio with increasing latitude.



565

566 **Figure 8.** a) North-south transect along the West African margin of dust flux records (black line;

567 McGee et al., 2013) and dust percentage records (purple line; Collins et al., 2013) b) Ratio of

568 Younger Dryas to Heinrich event 1 dust response versus latitude. All records were interpolated

569 to a resolution of 0.1 kyr, and a ratio of YD to H1 dust response was calculated using the

570 maximum value of the 0.5 kyr running means from within the time interval from 10.5-13.5 ka

571 (the Younger Dryas) and the time interval from 15-18 ka (Heinrich event 1). These broad

572 intervals were chosen in order to encompass age model uncertainty between the records.

573

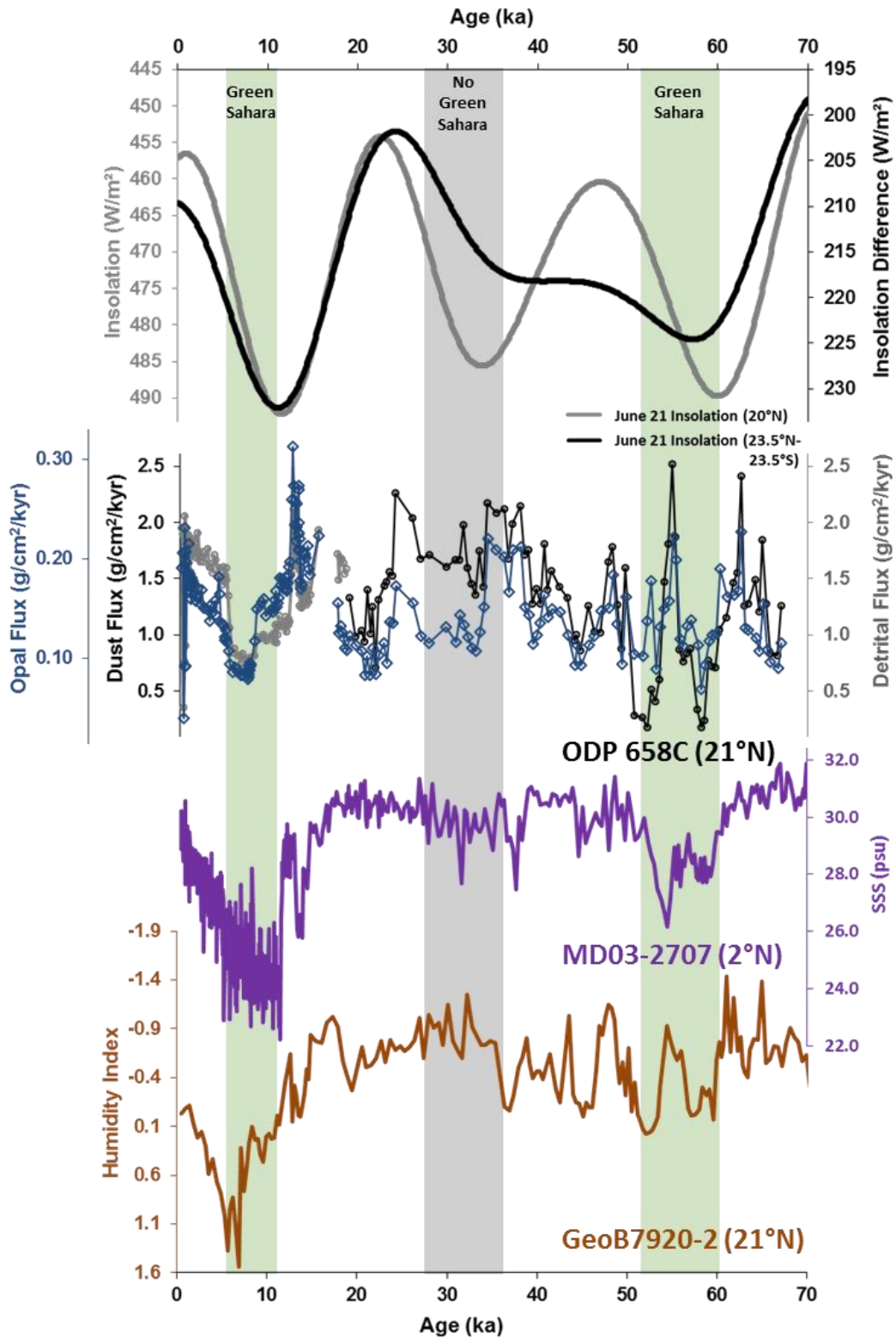
574 This observation suggests that northeasterly wind anomalies over North Africa peaked
575 south of 20°N in H1, and north of 20°N in the YD. This different atmospheric response may
576 reflect changing boundary conditions, and in particular smaller ice sheets in North America and
577 Europe, between H1 and the YD; alternatively, it may reflect differences in sea ice responses in
578 the two events. This difference in wind response in turn implies differences in the wind-driven
579 ocean circulation in the subtropical North Atlantic during the YD and H1.

580

581 4.4 Relationship Between Summer Insolation and NW African Climate During MIS 4 582 through 2

583 In the new extended ODP 658C dust record extremely low dust fluxes are observed
584 during the insolation maximum centered on 55 ka (Figure 9; low insolation values are oriented
585 upwards). The values seen in terms of detrital flux are even lower than those recorded during the
586 Green Sahara interval at 11 to 5 ka, where diverse proxy evidence indicates much higher rainfall
587 supporting diverse vegetation, permanent lakes, and human populations (Gasse, 2000; Jolly et al.,
588 1998; Kuper & Kröpelin, 2006; McGee & deMenocal, 2017; Tierney et al., 2017). Just as in the
589 AHP, opal fluxes are low, suggesting reduced northwesterly wind strength during this wet
590 period. The expression of the 60 to 50 ka low dust event differs from the AHP, however, in that
591 it is punctuated by an abrupt millennial-scale increase in dust at 55 ka associated with H5a. Dust
592 fluxes begin high at 60 ka ($1.5 \text{ g cm}^{-2} \text{ kyr}^{-1}$), decrease by a factor of three at 58 ka (0.5 g cm^{-2}
593 kyr^{-1}), increase dramatically at 55 ka ($2.5 \text{ g cm}^{-2} \text{ kyr}^{-1}$), and decrease to minimum values again at
594 52 ka ($0.5 \text{ g cm}^{-2} \text{ kyr}^{-1}$), before increasing gradually throughout the next 15 ka. This high dust
595 flux event indicates that high-latitude climate can exert a strong influence on African climate
596 even during a time of high summer insolation and a strong West African monsoon.

597



598 **Figure 9.** June 21 insolation at 20°N and cross-equatorial insolation gradient (calculated as the
599 difference in June 21 insolation between 23.5°N and 23.5°S) from Laskar et al., (2004) (dark
600 grey solid and dark grey dashed lines, respectively), ODP 658C dust and detrital flux records
601 (black and light grey lines with open circles, respectively), MD03-2707 sea surface salinity
602 (SSS) record, taken to reflect freshwater input from the Sanaga and Niger rivers to the eastern
603 Gulf of Guinea, from Weldeab et al., (2007) (purple line), and GeoB7920-2 Humidity Index
604 record from Tjallingii et al., (2008) (brown line). Data <20 ka in ODP 658C from Adkins et al.,
605 (2006).

606
607 Comparison of the dust flux record at 60 to 50 ka with other paleoclimate archives of
608 North African climate allows further probing of the structure of the Green Sahara event and how
609 the interplay of high-latitude climate forcing with high summer insolation affects North African
610 hydroclimate. The “W-shape” structure observed in the ODP 658C dust record is also observed
611 in sea surface salinity (SSS) reconstructions in the eastern Gulf of Guinea, taken to reflect
612 freshwater input from the Sanaga and Niger rivers, (Weldeab et al., 2007) and grain size-based
613 continental humidity reconstructions off Cape Blanc (Tjallingii et al., 2008) suggesting a wetter
614 tropical and subtropical North Africa. Wet conditions are also suggested by a low-resolution leaf
615 wax record from ODP 659, which shows quite depleted δD values at ~50 ka (Kuechler et al.,
616 2013).

617 The “W-shape” structure in the river discharge and humidity records differ somewhat
618 from the dust record, as they show wetter conditions following the 55 ka stadial event, while the
619 dust record shows equal magnitude dust flux minima preceding and following the stadial.
620 Further, the salinity and grain size records both suggest that the 60 to 50 ka wet period was
621 substantially drier than the Holocene AHP, while the detrital flux record of ODP 658C shows
622 values during the 60 to 50 ka time slice comparable to that of the 12 to 5 ka interval. Future work
623 will be required to explore the variable expression of this MIS 3 Green Sahara period in different
624 regions of North Africa using different proxies, and the reason for the extreme expression of the
625 AHP in many proxy records compared to earlier Green Sahara intervals. Potential avenues of
626 exploration include effects of bioturbation, smoothing due to higher frequency climatic events in
627 some intervals, and compaction of material downcore of the AHP leading to a bias in its
628 expression compared to other wet periods.

629 Dust export to ODP 658C during the local summer insolation maximum from 35 to 28 ka
630 has no discernible minimum in flux, as dust flux remains relatively high throughout this time,
631 unlike the dust minima seen during the previous insolation maximum/Green Sahara interval from
632 60 to 50 ka, and the following insolation maximum/Green Sahara interval from 12 to 5 ka. The
633 expression of this interval of insolation maximum (35 to 28 ka) in other records of North African
634 hydroclimate is also as a time of aridity, with very high sea surface salinity (interpreted as low
635 freshwater runoff from North Africa) in the Gulf of Guinea (Weldeab et al., 2007) and very low
636 humidity index (interpreted as a high ratio of aeolian to fluvial sediments) in sediments near
637 ODP 658C (Tjallingii et al., 2008). “Skipped beats” of insolation are similarly evident in the last
638 two glacial periods in a dust flux record from the northwest African margin (Skonieczny et al.,
639 2019) and a leaf wax δD records from East Africa (Tierney et al., 2017). In contrast, fluxes of
640 C_{org} and opal decrease by a factor of ~ 2 over this time interval (Figure 9), but do not reach the
641 minima observed in the Holocene and early MIS 3 Green Sahara intervals. This discrepancy,
642 with dust fluxes staying relatively high throughout the insolation maximum while biogenic
643 proxies decrease, may reflect a decrease in wind strength without a substantial decrease in
644 aridity. Alternatively, the reduced biogenic fluxes may result from changes in the nutrient
645 content of upwelled waters or effects on upwelling and productivity from changing shelf
646 morphology due to sea-level lowering.

647 The latter part of this arid interval is coincident with the coldest high latitude
648 temperatures during the past 70 ka as measured in Greenland ice, and the coldest North Atlantic
649 SSTs. The precessional beat of maximum local summer insolation at 35 to 28 ka thus occurs
650 during a colder interval with higher ice volume than the preceding and subsequent Green Sahara
651 intervals, suggesting that high latitude forcing during a time of high ice volume and cold
652 temperatures may override the impact of increased summer heating of North Africa on the
653 monsoon, keeping North Africa arid.

654 Alternatively, the lack of response to high local summer insolation at 35 to 28 ka could
655 be due to the fact that the precessional extreme occurs in association with low obliquity. As a
656 result, high latitude NH summer insolation and the cross-equatorial insolation gradient
657 (calculated as the difference in June 21 insolation between $23.5^{\circ}N$ and $23.5^{\circ}S$) remain low
658 despite the maximum in $20^{\circ}N$ summer insolation. We note that while much monsoon literature
659 has focused on $65^{\circ}N$ summer insolation, recent modeling experiments suggest that the cross-

660 equatorial insolation gradient (which varies in phase with 65°N insolation) is more directly
661 related to North African monsoon strength (Bosmans et al., 2015; Mantsis et al., 2014).

662 Modeling by Singarayer et al., (2017) appears to support the first suggestion. In their
663 simulations, the summer rain belt over North Africa reaches similar latitudes during the summer
664 insolation maxima at ~35 ka and ~55 ka when only orbital parameters and greenhouse gases are
665 changed, but the rain belt is substantially farther south at 35 ka when ice sheets are included in
666 the simulation.

667

668 **5 Conclusions**

669 Extended dust flux records from 19°N to 27°N along the West African margin show a
670 coherent signal of dust export during overlapping intervals, from 37 ka to present in cores GC37,
671 GC49, and ODP 658C, and additionally in core GC68 from 26 ka to present. These records show
672 a peak in dust at 35 to 33 ka, with fluxes decreasing throughout MIS 2; these multi-millennial
673 trends appear to correlate with high-latitude temperature changes indicated by Greenland ice
674 cores, with dust peaking during the coldest conditions. Due to the decline in dust fluxes in MIS
675 2, the LGM time slice commonly targeted in modeling experiments is marked by relatively
676 moderate dust fluxes. The existence of dust deposition similar to Late Holocene levels in most
677 cores despite the presence of large ice sheets and much steeper pole-to-equator surface
678 temperature gradients is worthy of further investigation.

679 There is also coherent millennial-scale variability throughout our records. In core GC68,
680 which has the highest accumulation rates and best-constrained age model in MIS 2, millennial-
681 scale dust peaks correspond with reductions in North Atlantic SSTs. At other sites, most stadial
682 events—including H2, H3, H5, H5a, and H6—correspond to periods of high dust fluxes. Due to
683 this strong coherence, we suggest that the few intervals in which high dust fluxes are not
684 observed at the same time as low SSTs result from age model errors and/or bioturbation.
685 Covariation of dust fluxes with fluxes of opal and organic carbon, taken here to represent coastal
686 upwelling intensity, suggests that dust flux peaks during stadials and are likely driven by
687 increases in northeasterly wind strength. This finding provides support for the role of
688 northeasterly winds in ventilating the West African monsoon during stadial events, leading to the
689 observed decreases in Sahel precipitation. Examining a broad suite of dust records along the
690 northwest African margin, we also find differences in wind anomalies associated with different

691 stadials, with wind anomalies peaking south of 20°N during H1 and north of 20°N during the
692 YD, perhaps due to changing ice sheet topography.

693 The longer dust flux record from ODP 658C reveals a “Green Sahara” interval at 60 to 50
694 ka marked by low dust fluxes. This period corresponds to a time of high NH summer insolation
695 and relatively warm North Atlantic SSTs, suggesting a strong West African monsoon even in the
696 presence of extended ice sheets and moderate atmospheric CO₂ concentrations. This interval
697 differs from the AHP (12 to 5 ka), as there is a millennial-scale peak in dust flux during the
698 interval that appears to correspond to H5a. The low latitude summer insolation maximum at 35
699 ka is a “skipped beat”, in that there is no record of a strengthening of the west African monsoon
700 and decrease in dust flux during this time, potentially due either to a reduced cross-equatorial
701 insolation gradient during this time of low obliquity, or to the influence of cold North Atlantic
702 temperatures and large ice sheets in counteracting the local insolation forcing on North African
703 climate.

704

705 **Acknowledgments, Samples, and Data**

706 The data supporting the conclusions is included in the Supporting Information as a separate
707 dataset for each core site for review purposes. This data is in the process of being archived and
708 will be submitted to the NOAA/WDS for Paleoclimatology archives by time of publication with
709 an in-text citation. We would like to thank I. Tal and E. Steponaitis at MIT for laboratory
710 assistance. We would also like to thank the crew, staff and scientists of R/V Oceanus cruise 437-
711 7, and co-chief scientists Tim Eglinton and Thomas Wagner. This research used samples
712 provided by the Ocean Drilling Program (ODP). This research was supported by NSF #OCE-
713 1103262 to L. Bradtmiller, NSF #OCE-1030784 to D. McGee, P. deMenocal and G. Winckler,
714 and by internal grants from Macalester College and MIT.

715

716 **References**

- 717 Adkins, J., deMenocal, P., & Eshel, G. (2006). The “African humid period” and the record of
718 marine upwelling from excess ²³⁰Th in Ocean Drilling Program Hole 658C.
719 *Paleoceanography*, 21(4), 1–14. <https://doi.org/10.1029/2005PA001200>
- 720 Andersen, M. B., Stirling, C. H., Zimmermann, B., & Halliday, A. N. (2010). Precise
721 determination of the open ocean ²³⁴U/²³⁸U composition. *Geochemistry, Geophysics*,

- 722 *Geosystems*, 11(12). <https://doi.org/10.1029/2010GC003318>
- 723 Bacon, M. P. (1984). Glacial to interglacial changes in carbonate and clay sedimentation in the
724 Atlantic Ocean estimated from ^{230}Th measurements. *Chemical Geology*, 46(2), 97–111.
725 [https://doi.org/10.1016/0009-2541\(84\)90183-9](https://doi.org/10.1016/0009-2541(84)90183-9)
- 726 Battisti, D. S., Ding, Q., & Roe, G. H. (2014). Coherent pan-Asian climatic and isotopic response
727 to orbital forcing of tropical insolation. *Journal of Geophysical Research*, 119(21), 11,997-
728 12,020. <https://doi.org/10.1002/2014JD021960>
- 729 Bory, A. J.-M., & Newton, P. P. (2000). Transport of airborne lithogenic material down through
730 the water column in two contrasting regions of the eastern subtropical North Atlantic
731 Ocean. *Global Biogeochemical Cycles*, 14(1), 297–315.
- 732 Bosmans, J. H. C., Drijfhout, S. S., Tuenter, E., Hilgen, F. J., & Lourens, L. J. (2015). Response
733 of the North African summer monsoon to precession and obliquity forcings in the EC-Earth
734 GCM. *Climate Dynamics*, 44(1–2), 279–297. <https://doi.org/10.1007/s00382-014-2260-z>
- 735 Braconnot, P., Harrison, S. P., Kageyama, M., Bartlein, P. J., Masson-Delmotte, V., Abe-Ouchi,
736 A., ... Zhao, Y. (2012). Evaluation of climate models using palaeoclimatic data. *Nature*
737 *Climate Change*, 2(6), 417–424. <https://doi.org/10.1038/nclimate1456>
- 738 Bradtmiller, L. I., McGee, D., Awalt, M., Evers, J., Yerxa, H., Kinsley, C. W., & deMenocal, P.
739 B. (2016). Changes in biological productivity along the northwest African margin over the
740 past 20,000 years. *Paleoceanography*, 31(1), 185–202.
741 <https://doi.org/10.1002/2015PA002862>
- 742 Bronk Ramsey, C. (2008). Deposition models for chronological records. *Quaternary Science*
743 *Reviews*, 27(1–2), 42–60. <https://doi.org/10.1016/j.quascirev.2007.01.019>
- 744 Cacho, I., Grimalt, J. O., Pelejero, C., Canals, M., Sierro, F. J., Flores, J. A., & Shackleton, N.
745 (1999). Dansgaard-Oeschger and Heinrich event imprints in Alboran Sea
746 paleotemperatures. *Paleoceanography*, 14(6), 698–705.
747 <https://doi.org/10.1029/1999PA900044>
- 748 Carlson, T. N., & Prospero, J. M. (1972). The Large-Scale Movement of Saharan Air Outbreaks
749 over the Northern Equatorial Atlantic. *Journal of Applied Meteorology*, 11, 283–297.
- 750 Chiapello, I., Bergametti, G., Gomes, L., Chatenet, B., Dulac, F., Pimenta, J., & Soares, E. S.
751 (1995). An additional low layer transport of Sahelian and Saharan dust over the north-
752 eastern Tropical Atlantic. *Geophysical Research Letters*, 22(23), 3191–3194.

- 753 <https://doi.org/10.1029/95GL03313>
- 754 Collins, J. A., Govin, A., Mulitza, S., Heslop, D., Zabel, M., Hartmann, J., ... Wefer, G. (2013).
755 Abrupt shifts of the Sahara-Sahel boundary during Heinrich stadials. *Climate of the Past*,
756 9(3), 1181–1191. <https://doi.org/10.5194/cp-9-1181-2013>
- 757 Copernicus Climate Change Service (C3S). (2017). ERA5: Fifth generation of ECMWF
758 atmospheric reanalyses of the global climate. Copernicus Climate Change Service Climate
759 Data Store (CDS). Retrieved May 22, 2020, from
760 <https://cds.climate.copernicus.eu/cdsapp#!/home>
- 761 deMenocal, P.B. (1995). Plio-Pleistocene African climate. *Science*, 270(5233), 53–59.
- 762 deMenocal, Peter B., Ortiz, J., Guilderson, T., Adkins, J., Sarnthein, M., Baker, L., &
763 Yarusinsky, M. (2000). Abrupt onset and termination of the African Humid Period: Rapid
764 climate responses to gradual insolation forcing. *Quaternary Science Reviews*, 19(1–5), 347–
765 361. [https://doi.org/10.1016/S0277-3791\(99\)00081-5](https://doi.org/10.1016/S0277-3791(99)00081-5)
- 766 deMenocal, Peter B., Ortiz, J., Guilderson, T., & Sarnthein, M. (2000). Coherent high- and low-
767 latitude climate variability during the holocene warm period. *Science*, 288(5474), 2198–
768 2202. <https://doi.org/10.1126/science.288.5474.2198>
- 769 deMenocal, Peter B., Ruddiman, W. F., & Pokras, E. M. (1993). Influences of High- and Low-
770 Latitude Processes on African Terrestrial Climate: Pleistocene Eolian Records from
771 Equatorial Atlantic Ocean Drilling Program Site 663. *Paleoceanography*, 8(2), 209–242.
772 <https://doi.org/10.1029/93PA02688>
- 773 Doherty, O. M., Riemer, N., & Hameed, S. (2012). Control of Saharan mineral dust transport to
774 Barbados in winter by the Intertropical Convergence Zone over West Africa. *Journal of*
775 *Geophysical Research Atmospheres*, 117(19), 1–13. <https://doi.org/10.1029/2012JD017767>
- 776 Drake, N. A., Blench, R. M., Armitage, S. J., Bristow, C. S., & White, K. H. (2010). Ancient
777 watercourses and biogeography of the Sahara explain the peopling of the desert.
778 *Proceedings of the National Academy of Sciences*, 1–5.
779 <https://doi.org/10.1073/pnas.1012231108>
- 780 Friese, C. A., van Hateren, J. A. Van, Vogt, C., Fischer, G., & Stuut, J.-B. W. (2017). Seasonal
781 provenance changes in present-day Saharan dust collected in and off Mauritania.
782 *Atmospheric Chemistry and Physics*, 17, 10163–10193. [https://doi.org/10.5194/acp-17-](https://doi.org/10.5194/acp-17-10163-2017)
783 10163-2017

- 784 Gasse, F. (2000). Hydrological changes in the African tropics since the Last Glacial Maximum.
785 *Quaternary Science Reviews*, 19(1–5), 189–211. [https://doi.org/10.1016/S0277-](https://doi.org/10.1016/S0277-3791(99)00061-X)
786 3791(99)00061-X
- 787 Gómez-Letona, M., Ramos, A. G., Coca, J., & Arístegui, J. (2017). Trends in Primary
788 Production in the Canary Current Upwelling System — A Regional Perspective Comparing
789 Remote Sensing Models. *Frontiers in Marine Science*, 4(November), 1–18.
790 <https://doi.org/10.3389/fmars.2017.00370>
- 791 Hayes, C. T., Anderson, R. F., Fleisher, M. Q., Huang, K., Robinson, L. F., Lu, Y., ... Moran, S.
792 B. (2015). Deep-Sea Research II Th and 231 Pa on GEOTRACES GA03 , the U . S .
793 GEOTRACES North Atlantic transect , and implications for modern and paleoceanographic
794 chemical fluxes. *Deep-Sea Research Part II*, 116, 29–41.
795 <https://doi.org/10.1016/j.dsr2.2014.07.007>
- 796 Holz, C., Stuut, J. B. W., & Henrich, R. (2004). Terrigenous sedimentation processes along the
797 continental margin off NW Africa: Implications from grain-size analysis of seabed
798 sediments. *Sedimentology*, 51(5), 1145–1154. [https://doi.org/10.1111/j.1365-](https://doi.org/10.1111/j.1365-3091.2004.00665.x)
799 3091.2004.00665.x
- 800 Holz, C., Stuut, J. B. W., Henrich, R., & Meggers, H. (2007). Variability in terrigenous
801 sedimentation processes off northwest Africa and its relation to climate changes: Inferences
802 from grain-size distributions of a Holocene marine sediment record. *Sedimentary Geology*,
803 202(3), 499–508. <https://doi.org/10.1016/j.sedgeo.2007.03.015>
- 804 Jolly, D., Prentice, I. C., Bonnefille, R., Ballouche, A., Bengo, M., Brenac, P., ... Waller, M.
805 (1998). Biome reconstruction from pollen and plant macrofossil data for Africa and the
806 Arabian peninsula at 0 and 6000 years. *Journal of Biogeography*, 25(6), 1007–1027.
807 <https://doi.org/10.1046/j.1365-2699.1998.00238.x>
- 808 Kuechler, R. R., Schefuß, E., Beckmann, B., Dupont, L., & Wefer, G. (2013). NW African
809 hydrology and vegetation during the Last Glacial cycle reflected in plant-wax-specific
810 hydrogen and carbon isotopes. *Quaternary Science Reviews*, 82, 56–67.
811 <https://doi.org/10.1016/j.quascirev.2013.10.013>
- 812 Kuper, R., & Kröpelin, S. (2006). Climate-controlled Holocene occupation in the Sahara: Motor
813 of Africa's evolution. *Science*, 313(5788), 803–807.
- 814 Kutzbach, J. E. (1981). Monsoon climate of the early Holocene: climate experiment with the

- 815 Earth's orbital parameters for 9000 years ago. *Science*, 214(OCTOBER), 59–61.
- 816 Laskar, J., Robutel, P., Joutel, F., Gastineau, M., Correia, A. C. M., & Levrard, B. (2004). Long-
817 term solution for the insolation quantities of the Earth. *Astronomy and Astrophysics*, (428),
818 261–285. <https://doi.org/10.1017/S1743921307011404>
- 819 Liu, Y., Chiang, J. C. H., Chou, C., & Patricola, C. M. (2014). Atmospheric teleconnection
820 mechanisms of extratropical North Atlantic SST influence on Sahel rainfall. *Climate*
821 *Dynamics*, 43(9–10), 2797–2811. <https://doi.org/10.1007/s00382-014-2094-8>
- 822 Locarnini, R. A., Mishonov, A. V., Baranova, O. K., Boyer, T. P., Zweng, M. M., Garcia, H. E.,
823 ... Smolyar, I. V. (2019). World Ocean Atlas 2018, Volume 1: Temperature. A. Mishonov,
824 Technical Editor. *NOAA Atlas NESDIS, 1(81)*, 52pp.
- 825 Mantsis, D. F., Lintner, B. R., Broccoli, A. J., Erb, M. P., Clement, A. C., & Park, H. S. (2014).
826 The response of large-scale circulation to obliquity-induced changes in meridional heating
827 gradients. *Journal of Climate*, 27(14), 5504–5516. [https://doi.org/10.1175/JCLI-D-13-](https://doi.org/10.1175/JCLI-D-13-00526.1)
828 00526.1
- 829 Martrat, B., Grimalt, J. O., Shackleton, N. J., De Abreu, L., Hutterli, M. A., & Stocker, T. F.
830 (2007). Four climate cycles of recurring deep and surface water destabilizations on the
831 Iberian margin. *Science*, 317(5837), 502–507. <https://doi.org/10.1126/science.1139994>
- 832 McGee, D., & deMenocal, P. B. (2017). *Climatic Changes and Cultural Responses During the*
833 *African Humid Period Recorded in Multi-Proxy Data* (Vol. 1). Oxford University Press.
834 <https://doi.org/10.1093/acrefore/9780190228620.013.529>
- 835 McGee, D., DeMenocal, P. B., Winckler, G., Stuut, J. B. W., & Bradtmiller, L. I. (2013). The
836 magnitude, timing and abruptness of changes in North African dust deposition over the last
837 20,000yr. *Earth and Planetary Science Letters*, 371–372, 163–176.
838 <https://doi.org/10.1016/j.epsl.2013.03.054>
- 839 McGee, D., Marcantonio, F., McManus, J. F., & Winckler, G. (2010). The response of excess
840 ^{230}Th and extraterrestrial ^3He to sediment redistribution at the Blake Ridge, western North
841 Atlantic. *Earth and Planetary Science Letters*, 299(1–2), 138–149.
842 <https://doi.org/10.1016/j.epsl.2010.08.029>
- 843 McGee, D., Moreno-Chamarro, E., Green, B., Marshall, J., Galbraith, E., & Bradtmiller, L.
844 (2018). Hemispherically asymmetric trade wind changes as signatures of past ITCZ shifts.
845 *Quaternary Science Reviews*, 180, 214–228.

- 846 <https://doi.org/10.1016/j.quascirev.2017.11.020>
- 847 Meyer, I., Davies, G. R., Vogt, C., Kuhlmann, H., & Stuut, J. B. W. (2013). Changing rainfall
848 patterns in NW Africa since the Younger Dryas. *Aeolian Research*, *10*, 111–123.
849 <https://doi.org/10.1016/j.aeolia.2013.03.003>
- 850 Middleton, J. L., Mukhopadhyay, S., Langmuir, C. H., McManus, J. F., & Huybers, P. J. (2018).
851 Millennial-scale variations in dustiness recorded in Mid-Atlantic sediments from 0 to 70 ka.
852 *Earth and Planetary Science Letters*, *482*, 12–22. <https://doi.org/10.1016/j.epsl.2017.10.034>
- 853 Mortlock, R. A., & Froelich, P. N. (1989). A simple method for the rapid determination of
854 biogenic opal in pelagic marine sediments. *Deep Sea Research Part A, Oceanographic
855 Research Papers*, *36*(9), 1415–1426. [https://doi.org/10.1016/0198-0149\(89\)90092-7](https://doi.org/10.1016/0198-0149(89)90092-7)
- 856 Mulitza, S., Heslop, D., Pittauerova, D., Fischer, H. W., Meyer, I., Stuut, J. B., ... Schulz, M.
857 (2010). Increase in African dust flux at the onset of commercial agriculture in the Sahel
858 region. *Nature*, *466*(7303), 226–228. <https://doi.org/10.1038/nature09213>
- 859 Mulitza, S., Prange, M., Stuut, J. B., Zabel, M., Von Dobeneck, T., Itambi, A. C., ... Wefer, G.
860 (2008). Sahel megadroughts triggered by glacial slowdowns of Atlantic meridional
861 overturning. *Paleoceanography*, *23*(4), 1–11. <https://doi.org/10.1029/2008PA001637>
- 862 Murphy, L. N., Clement, A. C., Albani, S., Mahowald, N. M., Swart, P., & Arienzo, M. M.
863 (2014). Simulated changes in atmospheric dust in response to a Heinrich stadial.
864 *Paleoceanography*, *29*(1), 30–43. <https://doi.org/10.1002/2013PA002550>
- 865 Ndeye, M. (2008). Marine reservoir ages in northern Senegal and Mauritania coastal waters.
866 *Radiocarbon*, *50*(2), 281–288. <https://doi.org/10.1017/S0033822200033580>
- 867 Pittauerov, D., Mulitza, S., Hettwig, B., Chehade, W., Stuut, J.-B., Mollenhauer, G., & Fischer,
868 H. W. (2009). Application of self-absorption correction method in gamma spectroscopy for
869 ²¹⁰Pb and ¹³⁷Cs sediment chronology on the continental slope off NW Africa .
870 *Radioprotection*, *44*(5), 457–461. <https://doi.org/10.1051/radiopro/20095085>
- 871 Prospero, J. M., & Lamb, P. J. (2003). African droughts and dust transport to the Caribbean:
872 climate change implications. *Science*, *302*(5647), 1024–1027.
873 <https://doi.org/10.1126/science.1089915>
- 874 Rasmussen, S. O., Andersen, K. K., Svensson, A. M., Steffensen, J. P., Vinther, B. M., Clausen,
875 H. B., ... Ruth, U. (2006). A new Greenland ice core chronology for the last glacial
876 termination. *Journal of Geophysical Research*, *111*, 1–16.

- 877 <https://doi.org/10.1029/2005JD006079>
- 878 Ratmeyer, V., Balzer, W., Bergametti, G., Chiapello, I., Fischer, G., & Wyputta, U. (1999).
879 Seasonal impact of mineral dust on deep-ocean particle flux in the eastern subtropical
880 Atlantic Ocean. *Marine Geology*, *159*, 241–252.
- 881 Reimer, P. J., Bard, E., Bayliss, A., Beck, J. W., Blackwell, P. G., Ramsey, C. B., ... van der
882 Plicht, J. (2013). IntCal13 and Marine13 Radiocarbon Age Calibration Curves 0–50,000
883 Years cal BP. *Radiocarbon*, *55*(04), 1869–1887. https://doi.org/10.2458/azu_js_rc.55.16947
- 884 Ridley, D. A., Heald, C. L., & Ford, B. (2012). North African dust export and deposition: A
885 satellite and model perspective. *Journal of Geophysical Research Atmospheres*, *117*(2), 1–
886 21. <https://doi.org/10.1029/2011JD016794>
- 887 Ridley, D. A., Heald, C. L., & Prospero, J. M. (2014). What controls the recent changes in
888 African mineral dust aerosol across the Atlantic? *Atmospheric Chemistry and Physics*,
889 *14*(11), 5735–5747. <https://doi.org/10.5194/acp-14-5735-2014>
- 890 Romero, O. E., Kim, J. H., & Donner, B. (2008). Submillennial-to-millennial variability of
891 diatom production off Mauritania, NW Africa, during the last glacial cycle.
892 *Paleoceanography*, *23*(3), 1–17. <https://doi.org/10.1029/2008PA001601>
- 893 Ruddiman, W., Sarnthein, M., Baldauf, J., Backman, J., Bloemendal, J., Curry, W., ... Yasuda,
894 H. (1988). *Proceedings of the Ocean Drilling Program Leg 108*.
- 895 Sánchez Goñi, M. F., & Harrison, S. P. (2010). Millennial-scale climate variability and
896 vegetation changes during the Last Glacial: Concepts and terminology. *Quaternary Science*
897 *Reviews*, *29*(21–22), 2823–2827. <https://doi.org/10.1016/j.quascirev.2009.11.014>
- 898 Scheuvens, D., Schütz, L., Kandler, K., Ebert, M., & Weinbruch, S. (2013). Earth-Science
899 Reviews Bulk composition of northern African dust and its source sediments — A
900 compilation. *Earth Science Reviews*, *116*, 170–194.
901 <https://doi.org/10.1016/j.earscirev.2012.08.005>
- 902 Seierstad, I. K., Abbott, P. M., Bigler, M., Blunier, T., Bourne, A. J., Brook, E., ... Vinther, B.
903 M. (2014). Consistently dated records from the Greenland GRIP, GISP2 and NGRIP ice
904 cores for the past 104ka reveal regional millennial-scale $\delta^{18}\text{O}$ gradients with possible
905 Heinrich event imprint. *Quaternary Science Reviews*, *106*, 29–46.
906 <https://doi.org/10.1016/j.quascirev.2014.10.032>
- 907 Singarayer, J. S., Valdes, P. J., & Roberts, W. H. G. (2017). Ocean dominated expansion and

- 908 contraction of the late Quaternary tropical rainbelt. *Scientific Reports*, 7(1), 1–9.
909 <https://doi.org/10.1038/s41598-017-09816-8>
- 910 Skonieczny, C., Bory, A., Bout-Roumazelles, V., Abouchami, W., Galer, S. J. G., Crosta, X., ...
911 Ndiaye, T. (2013). A three-year time series of mineral dust deposits on the West African
912 margin : Sedimentological and geochemical signatures and implications for interpretation of
913 marine paleo-dust records. *Earth and Planetary Science Letters*, 364, 145–156.
914 <https://doi.org/10.1016/j.epsl.2012.12.039>
- 915 Skonieczny, C., McGee, D., Winckler, G., Bory, A., Bradtmiller, L. I., Kinsley, C. W., ...
916 Malaizé, B. (2019). Monsoon-driven Saharan dust variability over the past 240,000 years.
917 *Science Advances*, 5(1), eaav1887. <https://doi.org/10.1126/sciadv.aav1887>
- 918 Skonieczny, C., Paillou, P., Bory, A., Bayon, G., Biscara, L., Crosta, X., ... Grousset, F. (2015).
919 African humid periods triggered the reactivation of a large river system in Western Sahara.
920 *Nature Communications*, 6, 6–11. <https://doi.org/10.1038/ncomms9751>
- 921 Stuut, J. B., Zabel, M., Ratmeyer, V., Helmke, P., Schefuß, E., Lavik, G., & Schneider, R.
922 (2005). Provenance of present-day eolian dust collected off NW Africa. *Journal of*
923 *Geophysical Research: Atmospheres*, 110(4), 1–14. <https://doi.org/10.1029/2004JD005161>
- 924 Suman, D. O., & Bacon, M. P. (1989). Variations in Holocene sedimentation in the North
925 American Basin determined from ^{230}Th measurements. *Deep Sea Research Part A,*
926 *Oceanographic Research Papers*, 36(6), 869–878. [https://doi.org/10.1016/0198-](https://doi.org/10.1016/0198-0149(89)90033-2)
927 [0149\(89\)90033-2](https://doi.org/10.1016/0198-0149(89)90033-2)
- 928 Sun, D. (2004). Monsoon and westerly circulation changes recorded in the late Cenozoic aeolian
929 sequences of Northern China. *Global and Planetary Change*, 41(1), 63–80.
930 <https://doi.org/10.1016/j.gloplacha.2003.11.001>
- 931 Tierney, J. E., deMenocal, P. B., & Zander, P. D. (2017). A climatic context for the out-of-Africa
932 migration. *Geology*, 45(11), 1023–1026. <https://doi.org/10.1130/G39457.1>
- 933 Tierney, J. E., Pausata, F. S. R., & De Menocal, P. B. (2017). Rainfall regimes of the Green
934 Sahara. *Science Advances*, 3(1), 1–10. <https://doi.org/10.1126/sciadv.1601503>
- 935 Tjallingii, R., Claussen, M., Stuut, J. B. W., Fohlmeister, J., Jahn, A., Bickert, T., ... Röhl, U.
936 (2008). Coherent high- and low-latitude control of the northwest African hydrological
937 balance. *Nature Geoscience*, 1(10), 670–675. <https://doi.org/10.1038/ngeo289>
- 938 van der Does, M., Korte, L. F., Munday, C. I., Brummer, G. J. A., & Stuut, J. B. W. (2016).

- 939 Particle size traces modern Saharan dust transport and deposition across the equatorial
 940 North Atlantic. *Atmospheric Chemistry and Physics*, 16(21), 13697–13710.
 941 <https://doi.org/10.5194/acp-16-13697-2016>
- 942 van der Jagt, H., Friese, C., Stuut, J.-B. W., Fischer, G., & Iversen, M. H. (2018). The ballasting
 943 effect of Saharan dust deposition on aggregate dynamics and carbon export: Aggregation,
 944 settling, and scavenging potential of marine snow. *Limnology and Oceanography*, 63,
 945 1386–1394. <https://doi.org/10.1002/lno.10779>
- 946 Waelbroeck, C., Labeyrie, L., Michel, E., Duplessy, J. C., McManus, J. F., Lambeck, K., ...
 947 Labracherie, M. (2002). Sea-level and deep water temperature changes derived from benthic
 948 foraminifera isotopic records. *Quaternary Science Reviews*, 21(1–3), 295–305.
 949 [https://doi.org/10.1016/S0277-3791\(01\)00101-9](https://doi.org/10.1016/S0277-3791(01)00101-9)
- 950 Waelbroeck, C., Paul, A., Kucera, M., Rosell-Melé, A., Weinelt, M., Schneider, R., ... Turon, J.
 951 L. (2009). Constraints on the magnitude and patterns of ocean cooling at the Last Glacial
 952 Maximum. *Nature Geoscience*, 2(2), 127–132. <https://doi.org/10.1038/ngeo411>
- 953 Wang, W., Evan, A. T., Flamant, C., & Lavaysse, C. (2015). On the decadal scale correlation
 954 between African dust and Sahel rainfall: The role of Saharan heat low-forced winds.
 955 *Science Advances*, 1(9), 2010–2015. <https://doi.org/10.1126/sciadv.1500646>
- 956 Weldeab, S., Lea, D. W., Schneider, R. R., & Andersen, N. (2007). 55,000 Years of West
 957 African Monsoon and Ocean Thermal Evolution. *Science*, 316(June), 1303–1306.
- 958 Weldeab, S., Menke, V., & Schmiedl, G. (2014). The pace of East African monsoon evolution
 959 during the Holocene. *Geophysical Research Letters*, (41), 1724–1731.
 960 <https://doi.org/10.1002/2014GL059361>
- 961 Williams, R. H., McGee, D., Kinsley, C. W., Ridley, D. A., Hu, S., Fedorov, A., ... deMenocal,
 962 P. B. (2016). Glacial to Holocene changes in trans-Atlantic Saharan dust transport and dust-
 963 climate feedbacks. *Science Advances*, 2(11), 1–12. <https://doi.org/10.1126/sciadv.1600445>
- 964 Yu, H., Chin, M., Bian, H., Yuan, T., Prospero, J. M., Omar, A. H., ... Zhang, Z. (2015). Remote
 965 Sensing of Environment Quantification of trans-Atlantic dust transport from seven-year (
 966 2007 – 2013) record of CALIPSO lidar measurements. *Remote Sensing of Environment*,
 967 159, 232–249. <https://doi.org/10.1016/j.rse.2014.12.010>
- 968 Zobeck, T. M., Gill, T. E., & Popham, T. W. (1999). A two-parameter Weibull function to
 969 describe airborne dust particle size distributions. *Earth Surface Processes and Landforms*,

970 955, 943–955. [https://doi.org/10.1002/\(SICI\)1096-9837\(199909\)24:10<943::AID-](https://doi.org/10.1002/(SICI)1096-9837(199909)24:10<943::AID-)
971 [ESP30>3.0.CO;2-9](https://doi.org/10.1002/(SICI)1096-9837(199909)24:10<943::AID-)
972